

# Verification of asymptotic homogenization method developed for periodic architected materials in strain gradient continuum

Hua Yang<sup>a</sup>, B. Emek Abali <sup>\*b</sup>, Wolfgang H. Müller <sup>a</sup>,  
Salma Barboura<sup>c</sup> and Jia Li<sup>c</sup>

<sup>a</sup>*Technische Universität Berlin, Berlin Germany*

<sup>b</sup>*Uppsala University, Uppsala, Sweden*

<sup>c</sup>*Sorbonne Paris North University, Paris, France*

## Abstract

Strain gradient theory is an accurate model for capturing the size effect and localization phenomena. However, the challenge in identification of corresponding constitutive parameters limits the practical application of the theory. We present and utilize asymptotic homogenization herein. All parameters in rank four, five, and six tensors are determined with the demonstrated computational approach. Examples for epoxy carbon fiber composite, metal matrix composite, and aluminum foam illustrate the effectiveness and versatility of the proposed method. The influences of volume fraction of matrix, the stack of RVEs, and the varying unit cell lengths on the identified parameters are investigated. The homogenization computational tool is applicable to a wide class materials and makes use of open-source codes in FEniCS. We make all of the codes publicly available in order to encourage a transparent scientific exchange.

*Keywords:* Strain gradient elasticity, Asymptotic homogenization method, Finite element method, constitutive parameters identification

## 1 Introduction

Composite materials have been widely used in engineering practice. Due to the heterogeneous nature of composites, the mechanical properties of such materials are dependent on their substructures, for example, the material properties of matrix and reinforcements, the shape of inclusions, or the volume fraction of matrix, etc. An accurate determination of effective properties of these heterogeneous media plays an important role in the design and analysis of composites. Experiments could be conceived to evaluate their effective properties, but it is also possible to compute effective material parameters by means of homogenization methods [1, 2], which reduce demands for experiments and enable to comprehend microstructure influence on the macroscale in any complex geometries.

Homogenization techniques [3, 4, 5, 6] allow to represent a heterogeneous elastic material, at the microscale, as an equivalent homogeneous elastic material at the macroscale. Although of primary importance, the conventional homogenization fails to describe the mechanical response when the heterogeneity of the material is of the same order of the macroscale. This inaccuracy is due to the fact that the conventional homogenization methods are based on a separation of scales, given by  $\epsilon = l/L$ ,  $l \ll L$ . Here,  $l$  represents the typical length scale characteristic of the microstructural heterogeneity and  $L$  stands for the macroscopic length scale. If the microstructure consists of relatively small heterogeneity, or the macroscopic length is infinitely large, classical homogenization gives an adequate estimate of the average macroscopic properties [7]. However, if the size of heterogeneity is of the same order of magnitude as that of the macroscopic problem, conventional homogenization technique fails. For example, the size effect occurs when the length scale of the macroscopic heterogeneous materials ( $L$ ) approaches the length scale of the underlying heterogeneity ( $l$ ). An up-scaling of Cauchy theory

---

\*Corresponding author: bilenemek@abali.org

indicates that additional terms are necessary in the constitutive equations in order to predict the size effect observed in experiments [8].

In order to incorporate these additional terms, different homogenization techniques are proposed in the literature, for example in the framework of generalized mechanics [9, 10, 11] such as micropolar theory [12, 13], couple stress [14], strain gradient theory [5, 15, 16, 17, 18, 19], and micromorphic continuum [20]. The task of obtaining homogenized constitutive equations for generalized continua is challenging and a number of debates are active in the literature [12, 13, 21, 22, 23]. Many methods have been proposed to construct strain gradient continua by means of asymptotic homogenization approaches [24, 25], multi-scale computational approaches [26], dynamic methods [27, 28], and several other identification techniques [29, 30, 31, 32, 33]. Asymptotic homogenization method improves descriptions by exploiting higher order terms and considering their role in macroscopic behaviors. In [34, 35, 36, 37, 38], an asymptotic homogenization based solution has been utilized to determine parameters of composite materials. Two issues were addressed therein. One is that the identified strain gradient parameters are all zero when structures are homogeneous. The other one is that these parameters are independent of stack of RVEs.

In this paper, we briefly recall the homogenization method described in [37], which is based on the formal analysis in [36]. A complete computational methodology determining all parameters in 2D and 3D has been achieved recently in [38]. We basically use the same procedure and verify the computational implementation by several numerical sanity checks. In this way, we reveal an important limitation that remains undetected during a formal analysis. Homogenization begins with two materials of different properties. In the case of one material with a nearly zero stiffness, the difference in properties may cause numerical problems in the implementation. For example, a structure with voids is a benchmark case for this issue. Indeed, we propose a change in the formulation in order to make the numerical implementation robust and the methodology more general. We apply the method to determine 2D and 3D composite materials effective parameters as well as verify the results by additional simulations. For determining parameters, we use epoxy carbon fiber composite material, SiC/Al metal matrix composite, and aluminum foam. As a benchmark, we choose aluminum foam.

The content of this paper is structured as follows: In Section 2, the underlying method is explained in order to clearly present the addition proposed herein. In Section 3, the details of a complete numerical implementation are demonstrated. In Section 4, effective parameters for 2D and 3D composite materials including epoxy-carbon fiber composites, metal matrix composite, and aluminum foam are identified as well as the aforementioned two challenges have been exploited for checking the robustness of the implementation. In Section 5 we discuss the positive definiteness and in Section 6 we verify the parameters by using a strain gradient simulation. The homogenization computational tool is developed based on open-source codes in FEniCS. It allows for all kinds of 2D or 3D composite materials constructed by periodic microstructures. The codes are made publicly available in [39] in order to enable a transparent scientific exchange.

## 2 Homogenization method

We start from an assertion that the deformation energy for the domain representing RVE,  $\Omega_P$ , at the microscale is equal to the energy for the RVE at the macroscale, namely

$$\int_{\Omega_P} w^m dV = \int_{\Omega_P} w^M dV . \quad (1)$$

The superscripts “m” and “M” are used to denote microscopic and macroscopic quantities, respectively. At the microscale, detailed microstructures are present in the RVE. At the macroscale, the same domain is modeled by a homogeneous “metamaterial.” We emphasize that an RVE may be different from a unit cell. A unit cell is the simplest repeating unit of heterogeneity. Spatial repetition of unit cells composes an RVE. At the microscale, the first order theory is used, as a consequence, we need to have a second order theory at the macroscale [40]. Now by starting with a linear strain measure, in the case of a linear material model, we obtain a quadratic deformation energy,

$$\int_{\Omega_P} \frac{1}{2} C_{ijkl}^m u_{i,j}^m u_{k,l}^m dV = \int_{\Omega_P} \left( \frac{1}{2} C_{ijkl}^M u_{i,j}^M u_{k,l}^M + G_{ijklm}^M u_{i,j}^M u_{k,lm}^M + \frac{1}{2} D_{ijklmn}^M u_{i,jk}^M u_{l,mn}^M \right) dV . \quad (2)$$

Displacement fields at micro- and macroscales are indicated by “m” and “M,” respectively.  $C_{ijkl}^m$  is given in each material point of the RVE. We begin with the known microscale and search for its corresponding homogenized effective parameters. The effective coefficients,  $C_{ijkl}^M$ ,  $G_{ijklm}^M$ , and  $D_{ijklmn}^M$  are the unknowns that we are searching for. We emphasize that the quadratic energy and symmetric strain measure lead to the minor

symmetries  $C_{ijkl}^m = C_{jikl}^m = C_{ijlk}^m, C_{ijkl}^M = C_{jikl}^M = C_{ijlk}^M, G_{ijklm}^M = G_{jiklm}^M = G_{ijlkm}^M, D_{ijklmn}^M = D_{jiklmn}^M = D_{ijkmln}^M$  and major symmetries  $C_{ijkl}^m = C_{klij}^m, C_{ijkl}^M = C_{klij}^M, D_{ijklmn}^M = D_{lmnijk}^M$  of the classical and strain gradient stiffness tensors. In what follows, the connections between the microscopic material parameters and macroscopic ones are established.

Let us investigate the macroscopic case for an RVE,  $\Omega_P$ . Firstly, the geometric center of the RVE is defined as  $\overset{c}{\mathbf{X}} = \frac{1}{V} \int_{\Omega_P} \mathbf{X} dV$ . A TAYLOR expansion of the macroscopic displacement around the center of the RVE is written as

$$\begin{aligned} u_i^M(\mathbf{X}) &= u_i^M \Big|_{\overset{c}{\mathbf{X}}} + u_{i,j}^M \Big|_{\overset{c}{\mathbf{X}}} (X_j - \overset{c}{X}_j) + \frac{1}{2} u_{i,jk}^M \Big|_{\overset{c}{\mathbf{X}}} (X_j - \overset{c}{X}_j)(X_k - \overset{c}{X}_k), \\ u_{i,i}^M(\mathbf{X}) &= u_{i,i}^M \Big|_{\overset{c}{\mathbf{X}}} \delta_{jl} + \frac{1}{2} u_{i,jk}^M \Big|_{\overset{c}{\mathbf{X}}} (\delta_{jl}(X_k - \overset{c}{X}_k) + (X_j - \overset{c}{X}_j)\delta_{kl}), \\ &= u_{i,i}^M \Big|_{\overset{c}{\mathbf{X}}} + u_{i,lk}^M \Big|_{\overset{c}{\mathbf{X}}} (X_k - \overset{c}{X}_k), \\ u_{i,lm}^M(\mathbf{X}) &= u_{i,lk}^M \Big|_{\overset{c}{\mathbf{X}}} \delta_{km} = u_{i,lm}^M \Big|_{\overset{c}{\mathbf{X}}}. \end{aligned} \quad (3)$$

Then by using the spatial averaging, we have

$$\begin{aligned} \langle u_{i,j}^M \rangle &= \frac{1}{V} \int_{\Omega_P} u_{i,j}^M dV = u_{i,j}^M \Big|_{\overset{c}{\mathbf{X}}}, \\ \langle u_{i,jk}^M \rangle &= \frac{1}{V} \int_{\Omega_P} u_{i,jk}^M dV = u_{i,jk}^M \Big|_{\overset{c}{\mathbf{X}}}. \end{aligned} \quad (4)$$

Therefore, the macroscopic energy of an RVE reads as follows (the detailed derivation can be found in [37]), as the macroscopic stiffness tensors are constant in space,

$$\begin{aligned} &\int_{\Omega_P} \left( \frac{1}{2} C_{ijkl}^M u_{i,j}^M u_{k,l}^M + G_{ijklm}^M u_{i,j}^M u_{k,lm}^M + \frac{1}{2} D_{ijklmn}^M u_{i,jk}^M u_{l,mn}^M \right) dV, \\ &= \frac{V}{2} C_{ijlm}^M \langle u_{i,j}^M \rangle \langle u_{l,m}^M \rangle + V G_{ijklm}^M \langle u_{i,j}^M \rangle \langle u_{k,lm}^M \rangle + \frac{V}{2} (C_{ijlm}^M \bar{I}_{kn} + D_{ijklmn}^M) \langle u_{i,jk}^M \rangle \langle u_{l,mn}^M \rangle, \end{aligned} \quad (5)$$

$$\bar{I}_{kn} = \frac{1}{V} \int_{\Omega_P} (X_k - \overset{c}{X}_k)(X_n - \overset{c}{X}_n) dV. \quad (6)$$

At the microscale, the asymptotic homogenization method is used to approximate the deformation energy for the RVE. We introduce a small parameter  $\epsilon$ , which is defined as  $\epsilon = \frac{l}{L}$ , where  $l$  is the characteristic length of the microstructure,  $L$  is the length of the macroscopic structure as shown in Fig. 1. We remark that  $\epsilon$  is the so-called homothetic ratio, which shows the scaling law for strain gradient moduli. This property will be illustrated later. A local coordinate is then introduced as

$$y_j = \frac{1}{\epsilon} (X_j - \overset{c}{X}_j), \quad (7)$$

which is used to describe the local fluctuations caused by microscopic heterogeneity. Variable  $\mathbf{X}$  is associated with the macroscopic scale. The displacement field for the RVE at the microscale is thus approximated with regard to  $\epsilon$  as

$$\mathbf{u}^m(\mathbf{X}) = \overset{0}{\mathbf{u}}(\mathbf{X}, \mathbf{y}) + \epsilon \overset{1}{\mathbf{u}}(\mathbf{X}, \mathbf{y}) + \epsilon^2 \overset{2}{\mathbf{u}}(\mathbf{X}, \mathbf{y}) + \dots \quad (8)$$

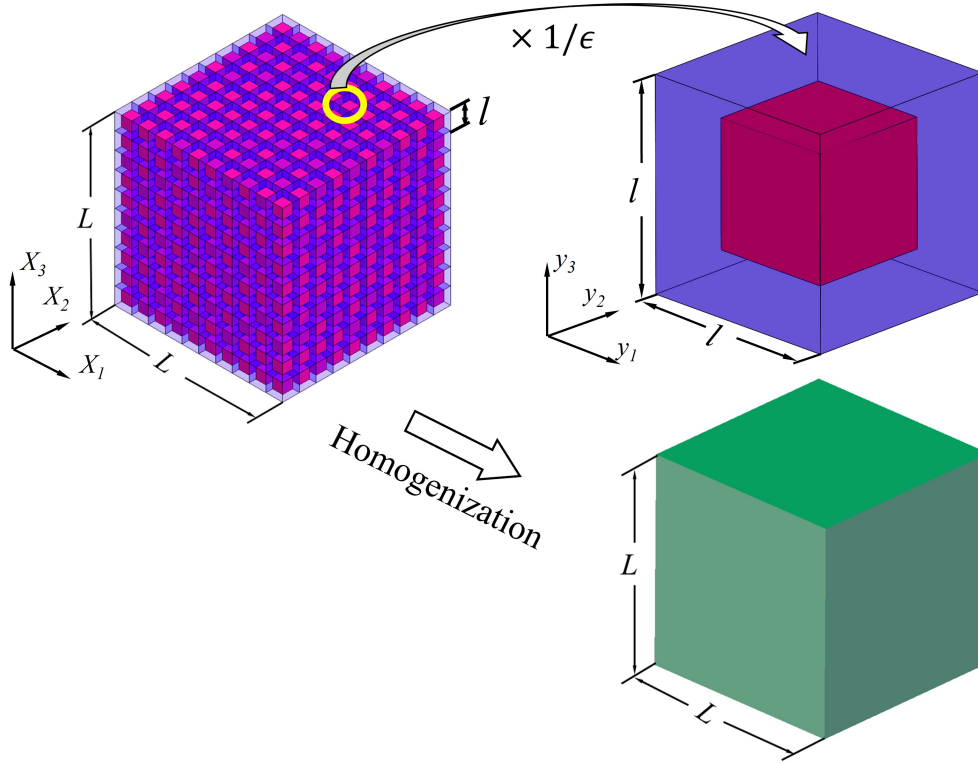


Figure 1: The heterogeneous continuum and its equivalent homogenized continuum.

For a linear elastostatics problem, we propose to write the governing equations within the RVE, as follows:

$$(C_{ijkl}^m u_{k,l}^m)_{,j} + \rho^m f_i = 0, \quad (9)$$

where  $\rho^m f_i$  are volume forces,  $\rho^m$  is the mass density at the microscale, hence it is a function in  $\mathbf{X}$  effected by the heterogeneous structure. We stress that this interpretation of using mass density at the microscale has an important remedy to the generality of the computational implementation. This change in the formulation is for the first time in the literature and numerically beneficial in the case of voids. Since voids possess numerically zero mass density, their contribution to the homogenization is weakened by exploiting this amendment in the formulation. By substituting Eqn. (8) to Eqn. (9) and gathering terms having the same order in  $\epsilon$  leads to the following equations:

- in the order of  $\epsilon^{-2}$

$$\frac{\partial}{\partial y_j} \left( C_{ijkl}^m \frac{\partial u_k^0}{\partial y_l} \right) = 0; \quad (10)$$

- in the order of  $\epsilon^{-1}$

$$\left( C_{ijkl}^m \frac{\partial u_k^0}{\partial y_l} \right)_{,j} + \frac{\partial}{\partial y_j} (C_{ijkl}^m u_{k,l}^0) + \frac{\partial}{\partial y_j} \left( C_{ijkl}^m \frac{\partial u_k^1}{\partial y_l} \right) = 0; \quad (11)$$

- in the order of  $\epsilon^0$

$$(C_{ijkl}^m u_{k,l}^0)_{,j} + \left( C_{ijkl}^m \frac{\partial u_k^1}{\partial y_l} \right)_{,j} + \frac{\partial}{\partial y_j} (C_{ijkl}^m u_{k,l}^1) + \frac{\partial}{\partial y_j} \left( C_{ijkl}^m \frac{\partial u_k^2}{\partial y_l} \right) + \rho^m f_i = 0. \quad (12)$$

The only possible solution of Eqn. (10) is to restrict  $u_i^0(\mathbf{X})$  as

$$u_i^0 = u_i^0(\mathbf{X}). \quad (13)$$

Because  $u_i^0(\mathbf{X})$  is only dependent on the macroscopic coordinates, from Eqn. (8), by a coefficient comparison, we obtain that it may be chosen as the macroscopic displacement  $u_i^0(\mathbf{X}) = u_i^M(\mathbf{X})$ . After substituting Eqn. (13)

into Eqn. (11), and introducing  $\varphi_{abc} = \varphi_{abc}(\mathbf{y})$  which is  $\mathbf{y}$ -periodic with zero average value  $\int_{\Omega^P} \varphi_{abi} dV = 0$ , we obtain

$$\frac{\partial}{\partial y_j} \left( C_{ijkl}^m \left( \frac{\partial \varphi_{abk}}{\partial y_l} + \delta_{ak} \delta_{bl} \right) \right) = 0 . \quad (14)$$

Consequently, the solution of Eqn. (11) is given as

$$\bar{u}_i = \varphi_{abi} u_{a,b}^M(\mathbf{X}) + \bar{u}_i(\mathbf{X}) , \quad (15)$$

where  $\bar{u}_i = \bar{u}_i(\mathbf{X})$  are integration constants.

By recalling the governing equation at the macroscale with an analogous suggestion to use a macroscale mass density, we have

$$C_{ijkl}^M u_{k,lj}^M - D_{ijklmn}^M u_{l,mnkj}^M + \rho^M f_i = 0 , \quad (16)$$

with  $\rho^M = \frac{1}{V} \int_{\Omega^P} \rho^m dV$  and the usual axiom that body forces are scale independent such that  $f_i$  remains the same at the micro- and macroscales. By neglecting the fourth order term in Eqn. (16), we obtain

$$f_i = - \frac{C_{ijkl}^M u_{k,lj}^M}{\rho^M} . \quad (17)$$

By plugging Eqn. (13), Eqn. (15) (with  $\bar{u}_i(\mathbf{X}) = 0$ ), and Eqn. (17) into Eqn. (12) and introducing  $\psi_{abci}$  which is  $\mathbf{y}$ -periodic with zero average  $\int_{\Omega^P} \psi_{abci} dV = 0$ , the solution of  $\bar{u}_i$  may be given as:

$$\bar{u}_i = \psi_{abci} u_{a,bc}^M(\mathbf{X}) + \bar{u}_i(\mathbf{X}) , \quad (18)$$

where  $\bar{u}_i(\mathbf{X})$  are integration constants in  $\mathbf{y}$ . The fourth order tensor  $\psi_{abcd}$  must satisfy

$$\frac{\partial}{\partial y_j} \left( C_{ijkl}^m \left( \frac{\partial \psi_{abck}}{\partial y_l} + \varphi_{abk} \delta_{lc} \right) \right) + C_{ickl}^m \left( \frac{\partial \varphi_{abk}}{\partial y_l} + \delta_{ka} \delta_{lb} \right) - \frac{\rho^m}{\rho^M} C_{icab}^M = 0 . \quad (19)$$

We emphasize that the last term is a source term simply applying the loading to the system at the microscale by considering mass densities. By neglecting the mass density ratio, one applies a source term even in the case of voids that may lead to numerically inconsistent results for  $\psi$  parameters. The microscale displacement field is rewritten as

$$u_i^m(\mathbf{X}, \mathbf{y}) = u_i^M(\mathbf{X}) + \epsilon \varphi_{abi}(\mathbf{y}) u_{a,b}^M(\mathbf{X}) + \epsilon^2 \psi_{abci}(\mathbf{y}) u_{a,bc}^M(\mathbf{X}) + \dots . \quad (20)$$

By using Eqn. (20) and the latter on the left-hand side of Eqn. (2) the microscopic energy becomes

$$\int_{\Omega^P} \frac{1}{2} C_{ijkl}^m u_{i,j}^m u_{k,l}^m dV = \frac{V}{2} \left( \bar{C}_{abcd} \langle u_{a,b}^M \rangle \langle u_{c,d}^M \rangle + \bar{G}_{abcde} \langle u_{a,b}^M \rangle \langle u_{c,de}^M \rangle + \bar{D}_{abcdef} \langle u_{a,bc}^M \rangle \langle u_{d,ef}^M \rangle \right) , \quad (21)$$

with

$$\begin{aligned} \bar{C}_{abcd} &= \frac{1}{V} \int_{\Omega^P} C_{ijkl}^m L_{abij} L_{cdkl} dV , \\ \bar{G}_{abcde} &= \frac{2\epsilon}{V} \int_{\Omega^P} C_{ijkl}^m L_{abij} M_{cdekl} dV \\ \bar{D}_{abcdef} &= \frac{\epsilon^2}{V} \int_{\Omega^P} C_{ijkl}^m M_{abcij} M_{defkl} dV , \end{aligned} \quad (22)$$

The appearance of  $\epsilon^2$  is due to the fact that Eqn. (26) is expressed in the local coordinate  $\mathbf{y}$  (The fifth order tensor  $\mathbf{M}$  is only related to  $\mathbf{y}$ ).

$$\begin{aligned} L_{abij} &= \delta_{ia} \delta_{jb} + \frac{\partial \varphi_{abi}}{\partial y_j} , \\ M_{abcij} &= y_c \left( \delta_{ia} \delta_{jb} + \frac{\partial \varphi_{abi}}{\partial y_j} \right) + \left( \varphi_{abi} \delta_{jc} + \frac{\partial \psi_{abci}}{\partial y_j} \right) . \end{aligned} \quad (23)$$

Based on Eqn. (2) the effective parameters are calculated by

$$C_{abcd}^M = \frac{1}{V} \int_{\Omega_P} C_{ijkl}^m L_{abij} L_{cdkl} dV , \quad (24)$$

$$G_{abcde}^M = \frac{\epsilon}{V} \int_{\Omega_P} C_{ijkl}^m L_{abij} M_{cdekl} dV , \quad (25)$$

$$D_{abcdef}^M = \frac{\epsilon^2}{V} \left( \int_{\Omega_P} C_{ijkl}^m M_{abcij} M_{defkl} dV - C_{abde}^M \int_{\Omega_P} y_c y_f dV \right) . \quad (26)$$

It should be remarked that the Eqn. (24) coincides with the well known asymptotic homogenization method. The classical stiffness tensor is scale independent. However, as observed from the Eqn. (26), strain gradient stiffness parameters depend on  $\epsilon^2$ . Indeed, these parameters emerge related to the substructure and vanish as  $\epsilon = 0$  meaning that the substructure diminishes. We stress that this distinction is of importance and comes out of the proposed methodology quite naturally. As obvious in Eqn. (7), the homothetic ratio,  $\epsilon$ , acts as a multiplier between the macroscopic length scale (in global coordinates,  $\mathbf{X}$ ) and microscopic length scale (in local coordinates,  $\mathbf{y}$ ). In this way, we acquire different  $\mathbf{G}^M$  and  $\mathbf{D}^M$  coefficients for the same RVE in larger structures without repeating the calculations. The role of  $\epsilon$  will be further illustrated by using numerical examples.

### 3 Numerical implementation

In order to identify effective parameters, Eqn. (24) and Eqn. (26) need to be resolved, which requires  $\varphi$  and  $\psi$ . The tensors  $\varphi$  and  $\psi$  are the solutions of Eqn. (14) and Eqn. (19), which are solved numerically by the finite element method. As shown in Figure 2, six cases  $\varphi_{11i}, \varphi_{22i}, \varphi_{33i}, \varphi_{23i}, \varphi_{13i}, \varphi_{12i}$  in total in 3D need to be computed under periodic boundary conditions. After using integration by parts, considering the constraints of zero average for  $\varphi$ , the following weak form for  $\varphi_{abk}$  is generated

$$\int_{\Omega^P} \left( C_{ijkl}^m \left( \frac{\partial \varphi_{abk}}{\partial y_l} + \delta_{ak} \delta_{bl} \right) \right) \frac{\partial \delta \varphi_{abi}}{\partial y_j} dV + \delta \int \lambda_{abi} \varphi_{abi} dV = 0 \quad (27)$$

and then immediately we have

$$\int_{\Omega^P} \left( C_{ijkl}^m \left( \frac{\partial \varphi_{abk}}{\partial y_l} + \delta_{ak} \delta_{bl} \right) \right) \frac{\partial \delta \varphi_{abi}}{\partial y_j} dV + \int_{\Omega^P} \lambda_{abi} \delta \varphi_{abi} dV + \int_{\Omega^P} \delta \lambda_{abi} \varphi_{abi} dV = 0 , \quad (28)$$

where over underlined indices, no summation convention is applied. All fields with a variational delta,  $\delta$ , denote a corresponding test function such that  $\varphi$  and  $\lambda$  are unknowns. For each case of  $\varphi_{11i}, \varphi_{22i}, \varphi_{33i}, \varphi_{23i}, \varphi_{13i}, \varphi_{12i}$ , a corresponding LAGRANGE multiplier  $\lambda_{11i}, \lambda_{22i}, \lambda_{33i}, \lambda_{23i}, \lambda_{13i}, \lambda_{12i}$ , is employed in order to enforce the zero average constrains of  $\varphi$  [41]. Likewise, the weak form for calculating  $\psi_{abci}$  reads

$$\begin{aligned} & \int_{\Omega^P} \left( \left( C_{ijkl}^m \left( \frac{\partial \psi_{abck}}{\partial y_l} + \varphi_{abk} \delta_{lc} \right) \right) \frac{\partial \delta \psi_{abci}}{\partial y_j} - \right. \\ & \left. - C_{iclk}^m \left( \frac{\partial \varphi_{abk}}{\partial y_l} + \delta_{ka} \delta_{lb} \right) \delta \psi_{abci} + \frac{\rho^m}{\rho^M} C_{icab}^M \delta \psi_{abci} \right) dV + \\ & + \int_{\Omega^P} \lambda_{abci} \delta \psi_{abci} dV + \int_{\Omega^P} \delta \lambda_{abci} \psi_{abci} dV = 0 . \end{aligned} \quad (29)$$

There are 18 weak forms in 3D to be solved for  $\psi_{111i}, \psi_{112i}, \dots, \psi_{123i}$ .

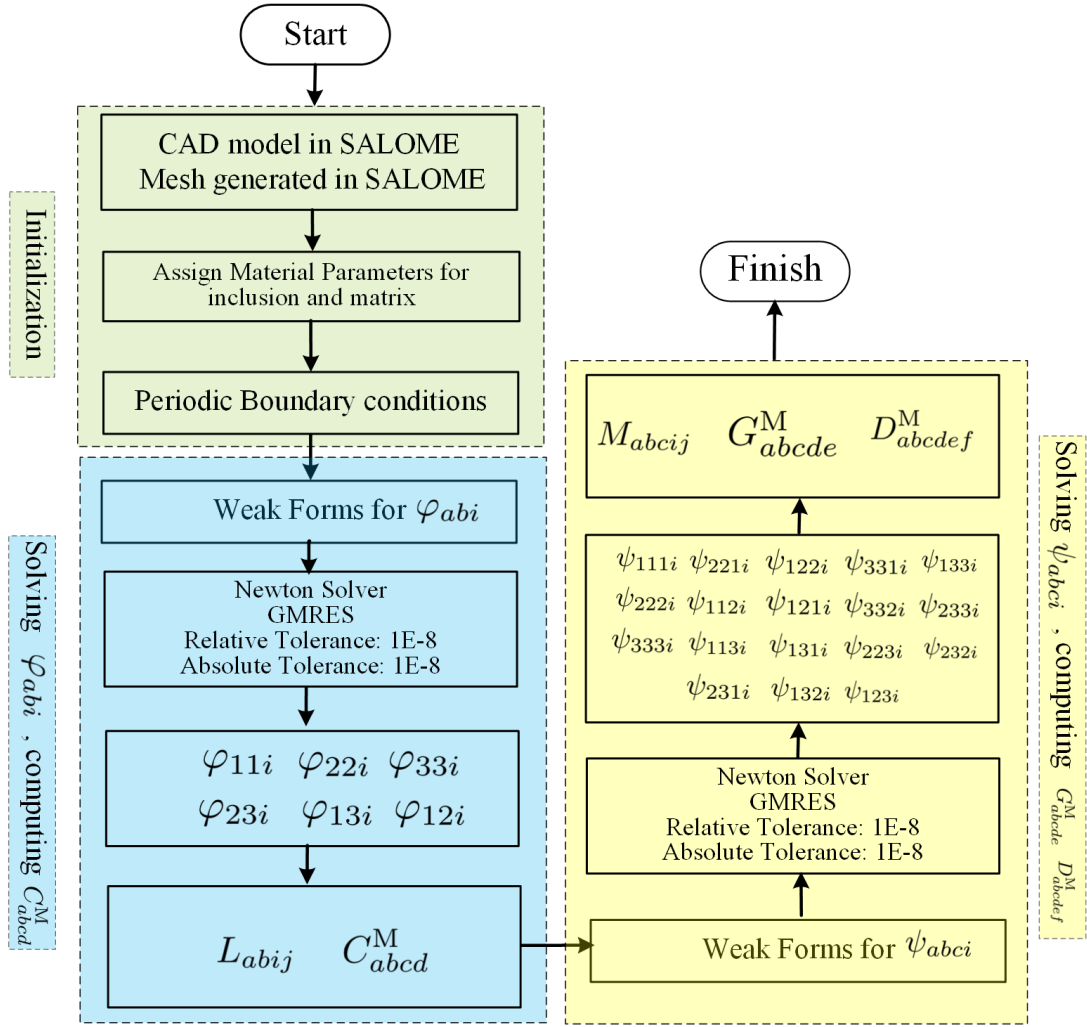


Figure 2: The flowchart of the numerical implementation.

The weak forms have been solved by the FEniCS platform. CAD model and mesh files are created by using an open-source software SALOME [42]. Triangle for surfaces elements and tetrahedron for volume elements are used to discretize the system by using the algorithms from NetGen Mesh Generator. An RVE needs to fulfill periodic boundary conditions such that the corresponding edges (in 2D) or surfaces (in 3D) are matching for nodes to be defined as the same degree of freedom in order to enforce the periodic boundary conditions as shown in Figure 3.

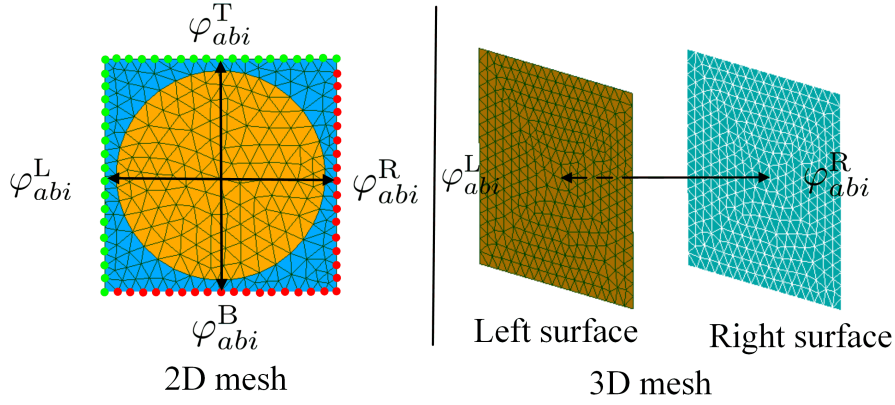


Figure 3: Periodic boundary conditions applied in FEM. Left: Right edge and green edge have the same mesh. Right: Only corresponding surfaces are shown, and so-called left surface and right surface have the same mesh. Same mesh is necessary for implementing periodic boundary conditions.

## 4 Numerical examples

The proposed homogenization method provides a unified analysis for general 2D and 3D composites. It may be used to homogenize fiber reinforced composites, particulate composites, and porous materials. In order to show the predictive capability of the proposed method, four examples are demonstrated in the following.

### 4.1 2D epoxy-carbon fiber composite

A 2 dimensional carbon fibers reinforced epoxy composite structure is investigated. The material properties <sup>1</sup> for both constituents (matrix and inclusion) are shown in Table 1. The size of the unit cell is 1 mm. The fiber is of circular shape, its radius is 0.45 mm, thus, the volume fraction of matrix is 36.4%.

Table 1: Material properties used for 2D epoxy-carbon fiber composite.  $E$  Young's modulus,  $\nu$  Poisson's ratio, and  $\rho$  mass density.

Type	$E$ in GPa	$\nu$	$\rho$ in kg/m <sup>3</sup>
Matrix (Epoxy)	17.3	0.35	1780
Inclusion (Carbon fiber)	35.9	0.30	1650

Voigt notations as presented in Table 2, Table 3 are used to represent rank four, five, six tensors as matrices (analogous to VOIGT's notation).

Table 2: VOIGT notation used for 2D strain tensors.

$A$	1	2	3
$ij$	11	22	12

Table 3: VOIGT kind-notation used for 2D strain-gradient tensors.

$\theta$	1	2	3	4	5	6
$ijk$	111	112	221	222	121	122

A bottleneck in the homogenization may be the missing convergence criteria. We propose a simple yet effective approach by using the material symmetry class of the analyzed microstructure. Owing to the cubic material

<sup>1</sup>Values of material properties are taken from matweb.com



symmetry, we know that  $C_{1111} = C_{2222}$ ,  $D_{111111} = D_{222222}$ . The convergence analysis is conducted as shown in Table 4, by comparing the ratios  $C_{1111}/C_{2222}$ , and  $D_{111111}/D_{222222}$ . When they tend to be 1, the computation is converged.

Table 4: Convergence analysis. With the increasing of degrees of freedom, the ratios  $C_{1111}/C_{2222}$ , and  $D_{111111}/D_{222222}$  reach 1.

DOFs	$C_{1111}$ GPa	$C_{2222}$ GPa	$C_{1111}/C_{2222}$	$D_{111111}$ N	$D_{222222}$ N	$D_{111111}/D_{222222}$
1342	38.6	38.7	99.7 %	510.4	496.0	103.0 %
22362	38.9	38.9	100.0 %	505.3	506.1	100.0 %
90226	39.0	39.0	100.0 %	506.4	505.8	100.0 %

The solutions for  $\varphi$  and  $\psi$  are presented in Figure 4. It is observed as expected that these fluctuations are all periodic. Furthermore, due to the fact that the material is cubic, rotating  $\varphi_{22}$ ,  $\psi_{111}$ ,  $\psi_{221}$ ,  $\psi_{122}$  by  $90^\circ$  gives the same shapes as  $\varphi_{11}$ ,  $\psi_{222}$ ,  $\psi_{112}$ ,  $\psi_{121}$ .

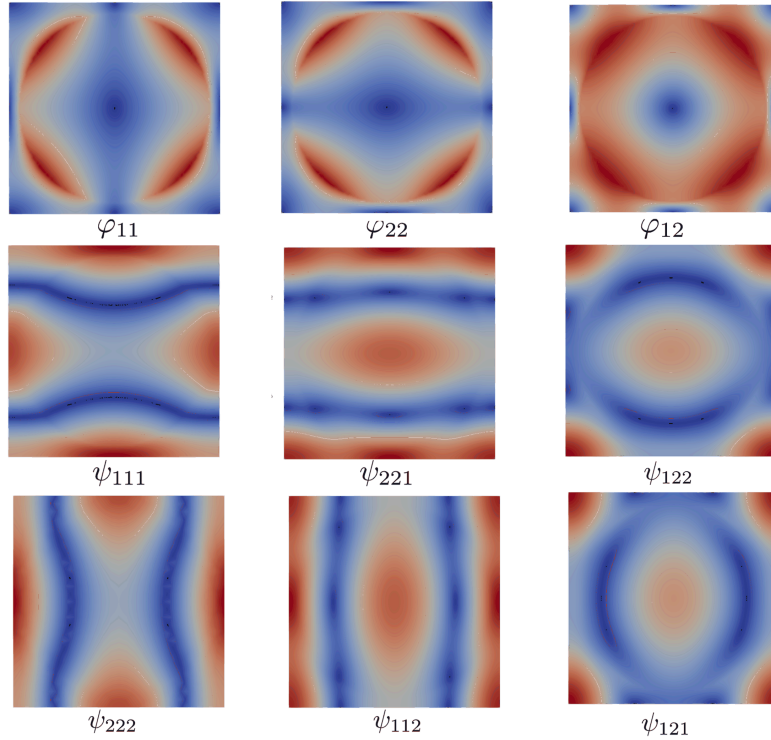


Figure 4: Solutions for  $\varphi$  and  $\psi$ . Color distribution showing the cubic symmetry resulted local fluctuation in  $\varphi$  and  $\psi$  fields. Color bars are omitted since we analyze qualitatively.

The identified effective classical and stain gradient stiffness tensors are shown as follows:

$$C_{AB}^M = \begin{pmatrix} 39.0 & 18.0 & 0.0 \\ 18.0 & 39.0 & 0.0 \\ 0.0 & 0.0 & 10.0 \end{pmatrix} \text{ GPa} ,$$

$$D_{\theta\gamma}^M = \begin{pmatrix} 506.4 & 181.9 & 0.0 & -0.0 & 0.0 & -182.2 \\ 181.9 & -299.4 & 0.0 & 0.0 & 0.0 & -176.2 \\ 0.0 & 0.0 & 181.2 & -175.4 & -183.0 & 0.0 \\ 0.0 & 0.0 & -175.4 & -298.5 & 181.2 & 0.0 \\ 0.0 & 0.0 & -183.0 & 181.2 & 505.8 & 0.0 \\ -182.2 & -176.2 & 0.0 & 0.0 & 0.0 & 181.0 \end{pmatrix} \text{ N} .$$

It is found that there are three independent parameters in the stiffness tensor and six independent parameters

in the strain gradient stiffness tensor. This observation is consistent with [43, 44] for cubic materials. Albeit we circumvent of showing, the implementation successfully computes all parameters of  $\mathbf{G}$  as (numerical) zeros, as expected from the cubic material symmetry as well. By using the VOIGT notation similar to the approach as in [43, 44, 45] in Table 5, the strain gradient stiffness matrix is made to be block-diagonal; each diagonal block matrix includes only non-zero parameters, and each diagonal block matrix is invariant under every cyclic permutation of  $\mathbf{X}$  axis,  $\mathbf{Y}$  axis, and  $\mathbf{Z}$  axis [45]. Therefore, the VOIGT notation proposed in [45] will be used throughout the paper.

Table 5: VOIGT notation used for 2D strain-gradient tensors proposed in [45].

$\alpha$	1	2	3	4	5	6
$ijk$	111	221	122	222	112	121

$$D_{\alpha\beta}^M = \begin{pmatrix} 506.4 & 181.9 & -182.2 & 0.0 & 0.0 & 0.0 \\ 181.9 & -299.4 & -176.2 & 0.0 & 0.0 & 0.0 \\ -182.2 & -176.2 & 181.0 & 0.0 & 0.0 & 0.0 \\ 0.0 & 0.0 & 0.0 & 505.8 & 181.2 & -183.0 \\ 0.0 & 0.0 & 0.0 & 181.2 & -298.5 & -175.4 \\ 0.0 & 0.0 & 0.0 & -183.0 & -175.4 & 181.2 \end{pmatrix} \text{N}.$$

## 4.2 Interpretation of the homothetic ratio

When determining the strain gradient moduli, physical relevance of the so-called homothetic ratio,  $\epsilon$ , is needed for determining the correct value. Two coordinate systems are scaled to each other by this homothetic ratio. Let us consider specific cases as shown in Figure 5. In Figure 5 (a), the macroscopic length is  $L = 4$  mm and the microscopic length is  $l = 1$  mm with  $\epsilon = \frac{l}{L} = \frac{1}{4}$ . RVE is of length  $L = 1$  mm in global coordinates  $\mathbf{X}$ , but it is measured as  $l = 4$  mm in local coordinate  $\mathbf{y}$ . Since Eqn. (26) are expressed in the local coordinate  $\mathbf{y}$ , the parameters in  $D_{abcdef}^M$  are calculated in the local coordinate. Thus, the length of the computational domain in Eqn. (26) is 4 mm. Likewise, in Figure 5 (b), the length of integration domain is 2 times larger than that in Figure 5 (a). However  $\epsilon = \frac{1}{8}$  is half of the former one. This leads to the equal values for strain gradient moduli. Consequently, in the last section,  $\epsilon$  can be chosen as, for example,  $\frac{1}{4}$  or  $\frac{1}{8}$ , as long as the corresponding length of integration domain is chosen accordingly.

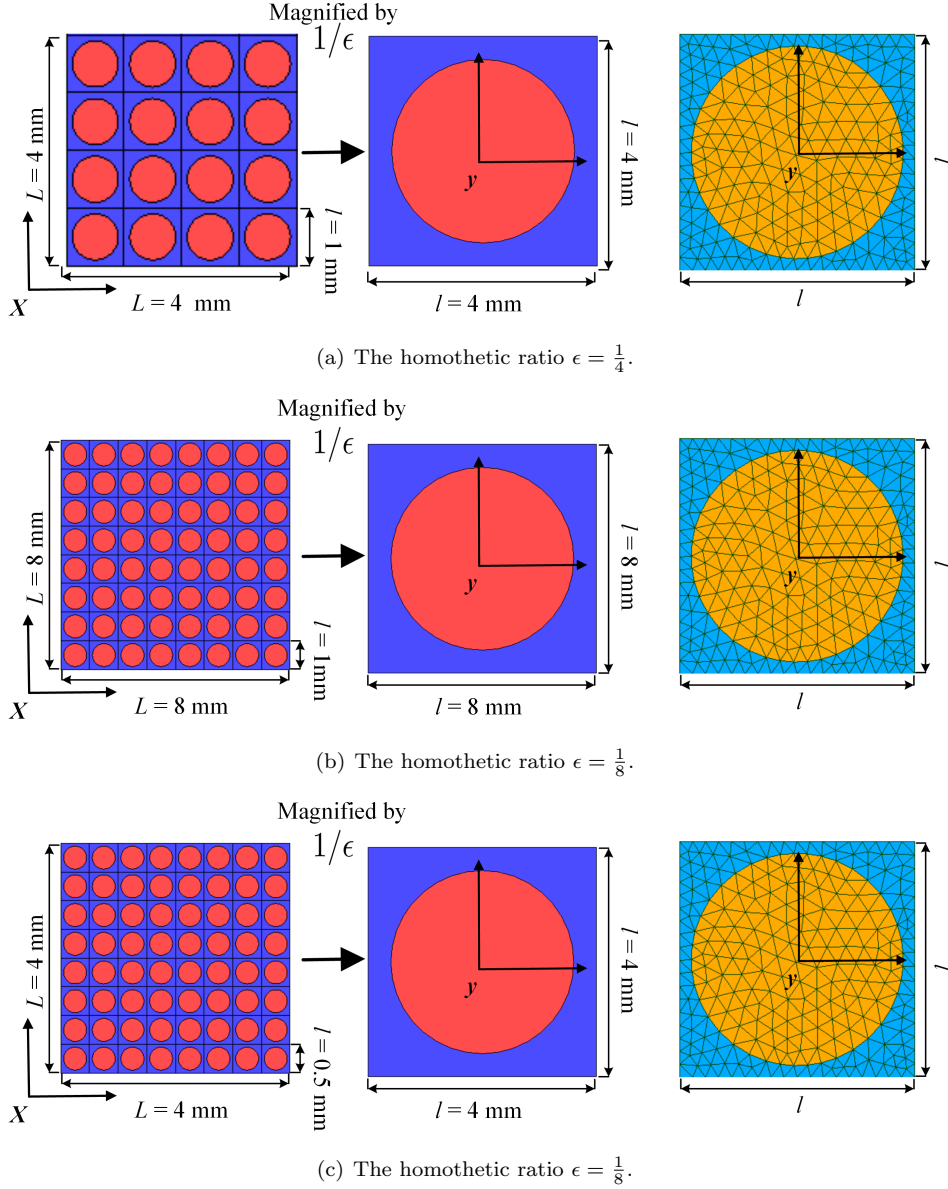


Figure 5: Visualization regarding the meaning of the homothetic ratio  $\epsilon$ .

Indeed, a scaling rule occurs for the strain gradient moduli. For example, in Figure 5 (c), the length of RVE is half of that in Figure 5 (a). The same macroscopic length equals calculated integrals in Eqn. (26). The differences of the obtained strain gradient parameters originate from the  $\epsilon^2$  as presented in Eqn. (26). The strain gradient parameters for Figure 5 (a) are 4 times larger than those for Figure 5 (c). This scaling factor is calculated as the ratio between  $\epsilon^2$ , also equal to the square of ratio of the unit cell lengths. Therefore, herein, we conclude that the strain gradient moduli are indeed not related to the macroscopic length but the microscopic length. This interpretation is indeed in coincidence with the well-known size effect in the literature. We emphasize that the substructure affects the values in  $C_{ijkl}^M$ , but not its ratio with respect to the macroscale. Therefore, for different substructures,  $C_{ijkl}^M$  needs to be recalculated. For the same substructure but different homothetic ratios, they remain the same.

### 4.3 3D cases

In the followings, we consider 3D cases. The effective parameters in the classical stiffness tensor and strain gradient stiffness tensor for a carbon fibers reinforced epoxy composite, a (hard) spherical particles reinforced (soft) matrix, a metal matrix composite, and an aluminum foam will be investigated. The used VOIGT notations for these 3 dimensional cases are displayed in Table 6 and Table 7.

Table 6: VOIGT notation used for 3D strain tensors.

$A$	1	2	3	4	5	6
$ij$	11	22	33	23	13	12

Table 7: VOIGT notation used for 3D strain-gradient tensors.

$\alpha$	1	2	3	4	5	6	7	8	9	10	11	12	13	14	15	16	17	18
$ijk$	111	221	122	331	133	222	112	121	332	233	333	113	131	223	232	231	132	123

### 4.3.1 3D fiber reinforced composite

Carbon fiber is modeled by using a cylindrical inclusion in 3D. In order to compare and validate the results, the same material properties shown in Table 1 are used for inclusion and matrix. The radius of the cylinder is of 0.45 mm so that the volume fraction of matrix reads 36.4 %, which are both equal to the example shown in 2D. The calculated parameters are shown as follows:

$$C_{AB}^M = \begin{pmatrix} 38.6 & 17.9 & 18.0 & 0.0 & 0.0 & 0.0 \\ 17.9 & 38.6 & 18.0 & 0.0 & 0.0 & 0.0 \\ 18.0 & 18.0 & 40.1 & 0.0 & 0.0 & 0.0 \\ 0.0 & 0.0 & 0.0 & 10.2 & 0.0 & 0.0 \\ 0.0 & 0.0 & 0.0 & 0.0 & 10.2 & 0.0 \\ 0.0 & 0.0 & 0.0 & 0.0 & 0.0 & 9.7 \end{pmatrix} \text{GPa} ,$$

$$D_{\alpha\beta}^M = \begin{pmatrix} 506.2 & 180.1 & -178.8 & 213.5 & 17.3 & 0.0 & 0.0 & 0.0 & 0.0 & 0.0 & 0.0 & 0.0 & 0.0 & 0.0 & 0.0 & 0.0 & 0.0 & 0.0 & 0.0 \\ 180.1 & -297.1 & -168.8 & -11.4 & -93.9 & 0.0 & 0.0 & 0.0 & 0.0 & 0.0 & 0.0 & 0.0 & 0.0 & 0.0 & 0.0 & 0.0 & 0.0 & 0.0 & 0.0 \\ -178.8 & -168.8 & 180.3 & -100.6 & -64.7 & 0.0 & 0.0 & 0.0 & 0.0 & 0.0 & 0.0 & 0.0 & 0.0 & 0.0 & 0.0 & 0.0 & 0.0 & 0.0 & 0.0 \\ 213.5 & -11.4 & -100.6 & -321.4 & -284.1 & 0.0 & 0.0 & 0.0 & 0.0 & 0.0 & 0.0 & 0.0 & 0.0 & 0.0 & 0.0 & 0.0 & 0.0 & 0.0 & 0.0 \\ 17.3 & -93.9 & -64.7 & -284.1 & 55.4 & 0.0 & 0.0 & 0.0 & 0.0 & 0.0 & 0.0 & 0.0 & 0.0 & 0.0 & 0.0 & 0.0 & 0.0 & 0.0 & 0.0 \\ 0.0 & 0.0 & 0.0 & 0.0 & 0.0 & 506.5 & 180.2 & -178.8 & 213.6 & 16.9 & 0.0 & 0.0 & 0.0 & 0.0 & 0.0 & 0.0 & 0.0 & 0.0 & 0.0 \\ 0.0 & 0.0 & 0.0 & 0.0 & 0.0 & 180.2 & -297.4 & -169.0 & -11.5 & -94.0 & 0.0 & 0.0 & 0.0 & 0.0 & 0.0 & 0.0 & 0.0 & 0.0 & 0.0 \\ 0.0 & 0.0 & 0.0 & 0.0 & 0.0 & -178.8 & -169.0 & 180.2 & -100.6 & -64.7 & 0.0 & 0.0 & 0.0 & 0.0 & 0.0 & 0.0 & 0.0 & 0.0 & 0.0 \\ 0.0 & 0.0 & 0.0 & 0.0 & 0.0 & 213.6 & -11.5 & -100.6 & -322.0 & -283.8 & 0.0 & 0.0 & 0.0 & 0.0 & 0.0 & 0.0 & 0.0 & 0.0 & 0.0 \\ 0.0 & 0.0 & 0.0 & 0.0 & 0.0 & 16.9 & -94.0 & -64.7 & -283.8 & 55.4 & 0.0 & 0.0 & 0.0 & 0.0 & 0.0 & 0.0 & 0.0 & 0.0 & 0.0 \\ 0.0 & 0.0 & 0.0 & 0.0 & 0.0 & 0.0 & 0.0 & 0.0 & 0.0 & 0.0 & 164.1 & 4.0 & -207.8 & 4.0 & -207.7 & 0.0 & 0.0 & 0.0 & 0.0 \\ 0.0 & 0.0 & 0.0 & 0.0 & 0.0 & 0.0 & 0.0 & 0.0 & 0.0 & 0.0 & 4.0 & 5.9 & 39.6 & -4.9 & -47.3 & 0.0 & 0.0 & 0.0 & 0.0 \\ 0.0 & 0.0 & 0.0 & 0.0 & 0.0 & 0.0 & 0.0 & 0.0 & 0.0 & 0.0 & -207.8 & 39.6 & 181.9 & -47.3 & -126.9 & 0.0 & 0.0 & 0.0 & 0.0 \\ 0.0 & 0.0 & 0.0 & 0.0 & 0.0 & 0.0 & 0.0 & 0.0 & 0.0 & 0.0 & 4.0 & -4.9 & -47.3 & 6.2 & 39.3 & 0.0 & 0.0 & 0.0 & 0.0 \\ 0.0 & 0.0 & 0.0 & 0.0 & 0.0 & 0.0 & 0.0 & 0.0 & 0.0 & 0.0 & -207.7 & -47.3 & -126.9 & 39.3 & 182.1 & 0.0 & 0.0 & 0.0 & 0.0 \\ 0.0 & 0.0 & 0.0 & 0.0 & 0.0 & 0.0 & 0.0 & 0.0 & 0.0 & 0.0 & 0.0 & 0.0 & 0.0 & 0.0 & 0.0 & 0.0 & -124.2 & -143.1 & -67.6 \\ 0.0 & 0.0 & 0.0 & 0.0 & 0.0 & 0.0 & 0.0 & 0.0 & 0.0 & 0.0 & 0.0 & 0.0 & 0.0 & 0.0 & 0.0 & 0.0 & -143.1 & -124.5 & -67.6 \\ 0.0 & 0.0 & 0.0 & 0.0 & 0.0 & 0.0 & 0.0 & 0.0 & 0.0 & 0.0 & 0.0 & 0.0 & 0.0 & 0.0 & 0.0 & 0.0 & -67.6 & -67.6 & 22.3 \end{pmatrix} \text{N} .$$

We stress that the algorithm computes  $\mathbf{G}$  as well, but as expected from the centro-symmetry in the substructure, all coefficients of  $\mathbf{G}$  vanish. The unidirectional laminate carbon reinforced epoxy composite is a transverse isotropic material. There are five independent parameters in the classical stiffness tensor, as shown below

$$C_{AB}^M = \begin{pmatrix} c_1 & c_1 - 2c_5 & c_2 & 0.0 & 0.0 & 0.0 \\ c_1 - 2c_5 & c_1 & c_2 & 0.0 & 0.0 & 0.0 \\ c_2 & c_2 & c_3 & 0.0 & 0.0 & 0.0 \\ 0.0 & 0.0 & 0.0 & c_4 & 0.0 & 0.0 \\ 0.0 & 0.0 & 0.0 & 0.0 & c_4 & 0.0 \\ 0.0 & 0.0 & 0.0 & 0.0 & 0.0 & c_5 \end{pmatrix} .$$

We stress that the computed parameters are satisfying this condition within a tolerance of  $\pm 6.7\%$ . After investigating the strain gradient stiffness tensor, we find the relations between higher order parameters as shown in Figure 6.

$D_{111111}$	$D_{111221}$	$D_{111122}$	$D_{111331}$	$D_{111333}$	0	0	0	0	0	0	0	0	0	0	0	0	0	0	
	$D_{221221}$	$D_{221122}$	$D_{221331}$	$D_{221333}$	0	0	0	0	0	0	0	0	0	0	0	0	0	0	
		$D_{122122}$	$D_{122331}$	$D_{122133}$	0	0	0	0	0	0	0	0	0	0	0	0	0	0	
			$D_{331331}$	$D_{331133}$	0	0	0	0	0	0	0	0	0	0	0	0	0	0	
			$D_{133133}$	0	0	0	0	0	0	0	0	0	0	0	0	0	0	0	
				$D_{222222}$	$D_{222112}$	$D_{222121}$	$D_{222332}$	$D_{222333}$	0	0	0	0	0	0	0	0	0	0	
					$D_{112112}$	$D_{112121}$	$D_{112332}$	$D_{112233}$	0	0	0	0	0	0	0	0	0	0	
						$D_{121212}$	$D_{121332}$	$D_{121233}$	0	0	0	0	0	0	0	0	0	0	
							$D_{332332}$	$D_{332233}$	0	0	0	0	0	0	0	0	0	0	
							$D_{233233}$	0	0	0	0	0	0	0	0	0	0	0	
								$D_{333333}$	$D_{333113}$	$D_{333131}$	$D_{333223}$	$D_{333232}$	0	0	0	0	0	0	
									$D_{113113}$	$D_{113131}$	$D_{113223}$	$D_{113232}$	0	0	0	0	0	0	
										$D_{131131}$	$D_{131223}$	$D_{131232}$	0	0	0	0	0	0	
											$D_{232232}$	$D_{232323}$	0	0	0	0	0	0	
												$D_{233232}$	0	0	0	0	0	0	
													$D_{231231}$	$D_{231132}$	$D_{231233}$	0	0	0	
														$D_{132132}$	$D_{132123}$	0	0	0	
															$D_{123123}$	0	0	0	
																$D_{123123}$	0	0	0

Sym.

Figure 6: The structure of strain gradient stiffness tensor for transverse isotropic materials. It is found that the first two  $5 \times 5$  matrices in the diagonal are equal, for example,  $D_{111111} = D_{222222}$ . In the third  $5 \times 5$  matrix in the diagonal, it is also observed that  $D_{333113} = D_{333223}$ ,  $D_{333131} = D_{333232}$ ,  $D_{113113} = D_{223223}$ ,  $D_{113131} = D_{223232}$ ,  $D_{113232} = D_{131223}$ ,  $D_{131131} = D_{232232}$ . In the  $3 \times 3$  matrix,  $D_{231231} = D_{132132}$ ,  $D_{231123} = D_{132123}$ .

Excluding the parameters of the same value, there are 28 parameters in  $\mathbf{D}$  for this transverse isotropic material

$$D_{\alpha\beta}^M = \begin{pmatrix} d_1 & d_2 & d_3 & d_4 & d_5 & 0 & 0 & 0 & 0 & 0 & 0 & 0 & 0 & 0 & 0 & 0 & 0 & 0 & 0 \\ & d_6 & d_7 & d_8 & d_9 & 0 & 0 & 0 & 0 & 0 & 0 & 0 & 0 & 0 & 0 & 0 & 0 & 0 & 0 \\ & & d_{10} & d_{11} & d_{12} & 0 & 0 & 0 & 0 & 0 & 0 & 0 & 0 & 0 & 0 & 0 & 0 & 0 & 0 \\ & & & d_{13} & d_{14} & 0 & 0 & 0 & 0 & 0 & 0 & 0 & 0 & 0 & 0 & 0 & 0 & 0 & 0 \\ & & & & d_{15} & 0 & 0 & 0 & 0 & 0 & 0 & 0 & 0 & 0 & 0 & 0 & 0 & 0 & 0 \\ & & & & & d_1 & d_2 & d_3 & d_4 & d_5 & 0 & 0 & 0 & 0 & 0 & 0 & 0 & 0 & 0 \\ & & & & & & d_6 & d_7 & d_8 & d_9 & 0 & 0 & 0 & 0 & 0 & 0 & 0 & 0 & 0 \\ & & & & & & & d_{10} & d_{11} & d_{12} & 0 & 0 & 0 & 0 & 0 & 0 & 0 & 0 & 0 \\ & & & & & & & & d_{13} & d_{14} & 0 & 0 & 0 & 0 & 0 & 0 & 0 & 0 & 0 \\ & & & & & & & & & d_{15} & 0 & 0 & 0 & 0 & 0 & 0 & 0 & 0 & 0 \\ & & & & & & & & & & d_{16} & d_{17} & d_{18} & d_{17} & d_{18} & 0 & 0 & 0 & 0 \\ & & & & & & & & & & & d_{19} & d_{20} & d_{21} & d_{22} & 0 & 0 & 0 & 0 \\ & & & & & & & & & & & & d_{23} & d_{22} & d_{24} & 0 & 0 & 0 & 0 \\ & & & & & & & & & & & & & d_{19} & d_{20} & 0 & 0 & 0 & 0 \\ & & & & & & & & & & & & & & d_{23} & 0 & 0 & 0 & 0 \\ & & & & & & & & & & & & & & & d_{25} & d_{27} & d_{28} & \\ & & & & & & & & & & & & & & & & d_{25} & d_{28} & \\ & & & & & & & & & & & & & & & & & d_{26} & \end{pmatrix}.$$

Sym.

We emphasize that some of the 28 parameters could be linearly dependent that leads to a reduction of independent coefficients. Moreover, the corresponding parameters in 2D and 3D stiffness tensors are equal within a tolerance of  $\pm 4.4\%$ , for example,  $C_{1111}$  or  $D_{111111}$  in the 2D stiffness tensors are equal to those in the 3D tensors. This verifies the calculated results. In order to further examine the homogenization method, computations for different volume fraction of matrix are conducted as presented in Figure 7.

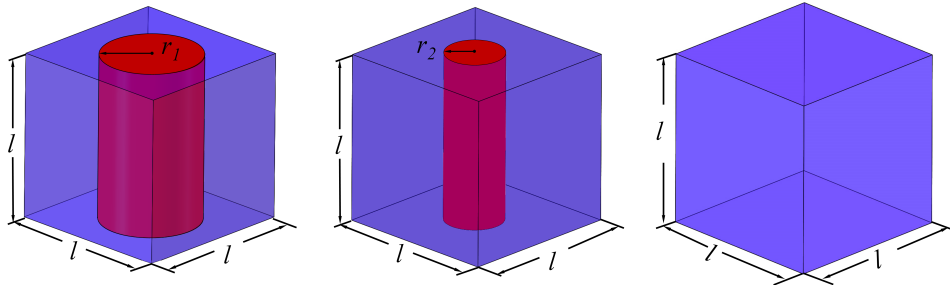


Figure 7: Different volume fraction of matrix.  $l = 1$  mm,  $r_1 = 0.45$  mm,  $r_2 = 0.35$  mm.

The results are shown in Figure 8. It is observed that with the increasing of the volume fraction of matrix, absolute values of most of effective parameters decrease. This is due to the fact that matrix (epoxy) is softer than inclusion (carbon). It should be emphasized that when the volume fraction of matrix is 1, namely the material is purely homogeneous, the higher order parameters vanish as expected.

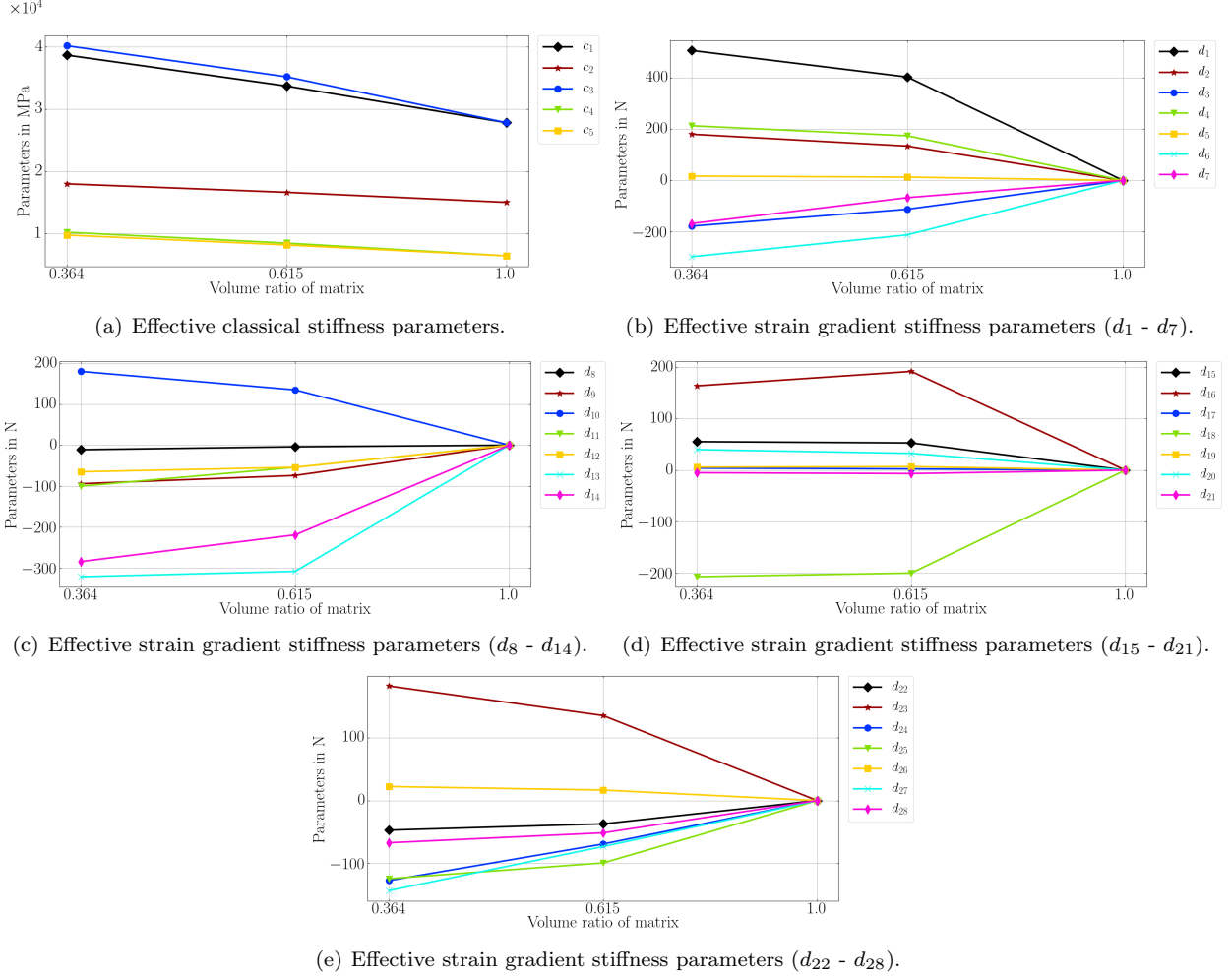


Figure 8: Effective material parameters with the changing of volume fraction of matrix. It should be noted that when the material is purely homogeneous (volume fraction of matrix is 1), all higher order parameters vanish.

Further investigations are carried out for RVEs by varying their sizes ( $1\text{ mm} \times 1\text{ mm} \times 1\text{ mm}$  and  $2\text{ mm} \times 2\text{ mm} \times 2\text{ mm}$  as well as  $3\text{ mm} \times 3\text{ mm} \times 3\text{ mm}$ ) as shown in Figure 9 and Figure 10. It is found that all coefficients remain constant, which indicates that the obtained parameters are independent of the repetition of RVEs.

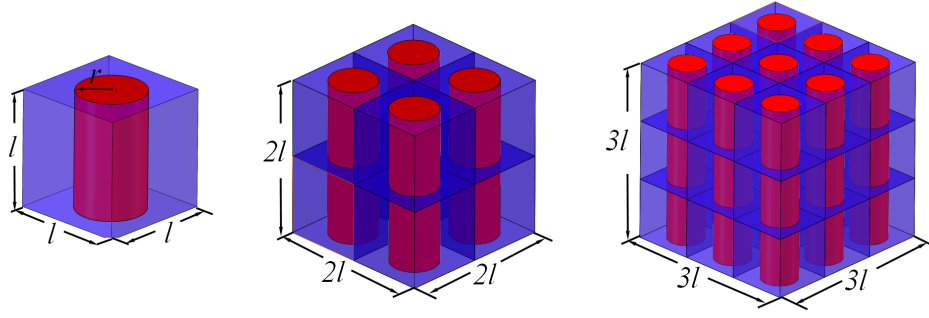


Figure 9: RVEs constructed by 1 unit cell, 8 unit cells, 27 unit cells.  $l = 1$  mm, the radius of fiber is 0.45 mm.

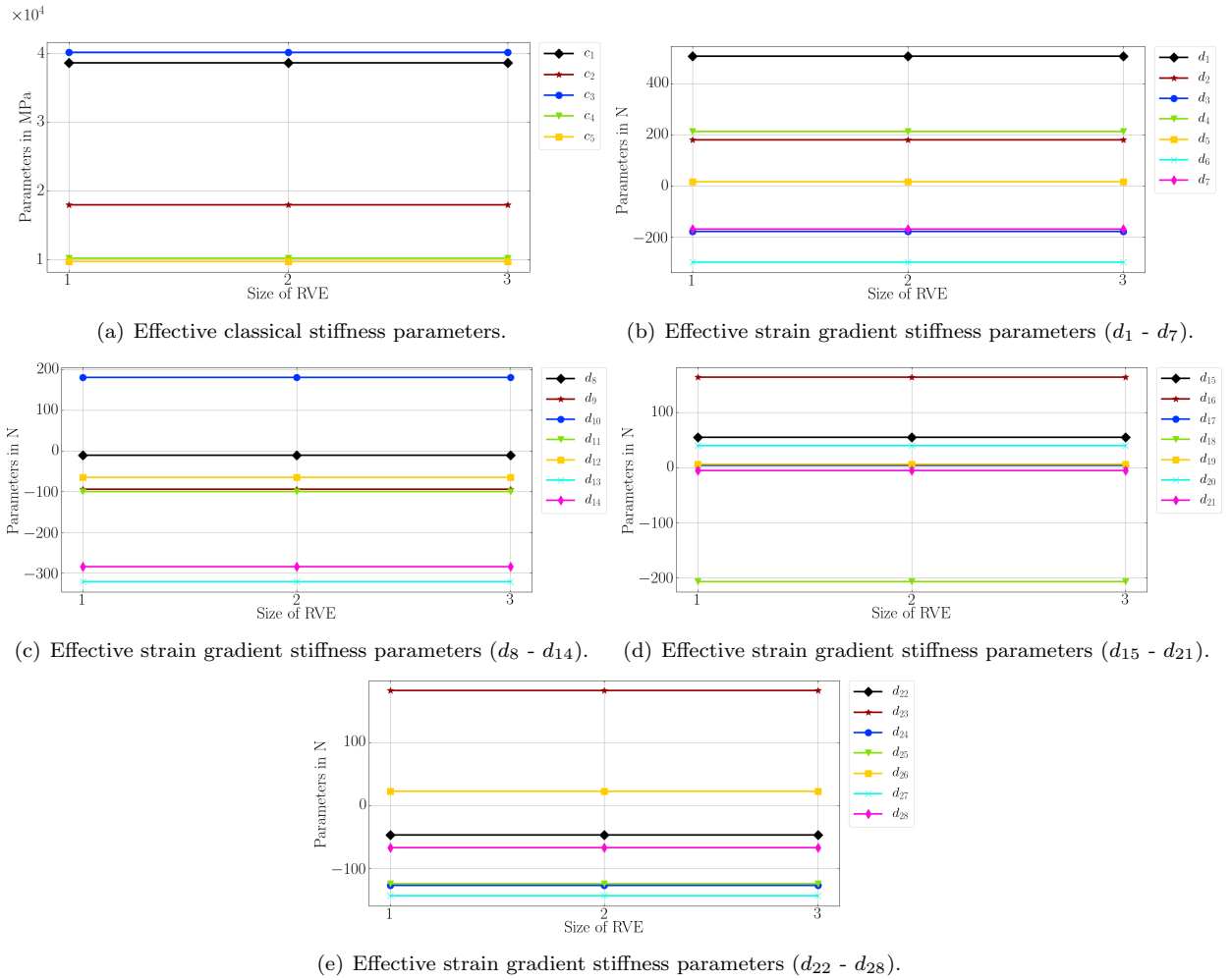


Figure 10: Effective material parameters with the repetition of RVEs (1 mm  $\times$  1 mm  $\times$  1 mm, 2 mm  $\times$  2 mm  $\times$  2 mm, 3 mm  $\times$  3 mm  $\times$  3 mm ).

Effective parameters are studied for unit cells with varying sizes as displayed in Figure 11. The smaller unit cells are generated by homothetically scaling the larger one. Therefore, the volume fraction of matrix is identical in these cases. It is found in Figure 12 that the parameters in the classical stiffness tensor remain the same, but the ones in the strain gradient stiffness tensor vary by changing the unit cell lengths. This fact is because of  $C_{ijkl}^M$  being invariant regarding the microstructural size. However the effective strain gradient ones are sensitive to the homothetic ratio  $\epsilon$ . These higher order parameters follow a scaling rule. For example, the parameters can be obtained for the unit cell size of 0.5 mm  $\times$  0.5 mm  $\times$  0.5 mm by multiplying a scaling factor with the effective parameters of the unit cell size of 1 mm  $\times$  1 mm  $\times$  1 mm. The scaling factor is the square of homothetic

ratio  $\epsilon^2$ , which is numerically equal to the square of ratio of the unit cell lengths herein.

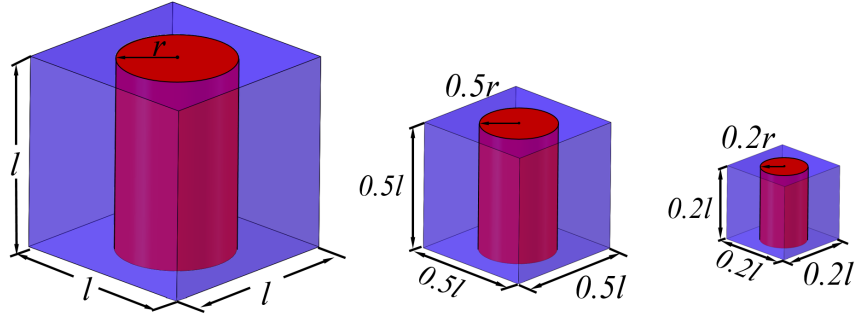


Figure 11: Unit cells with the changing sizes.  $l = 1$  mm The volume fraction of matrix are kept equal.

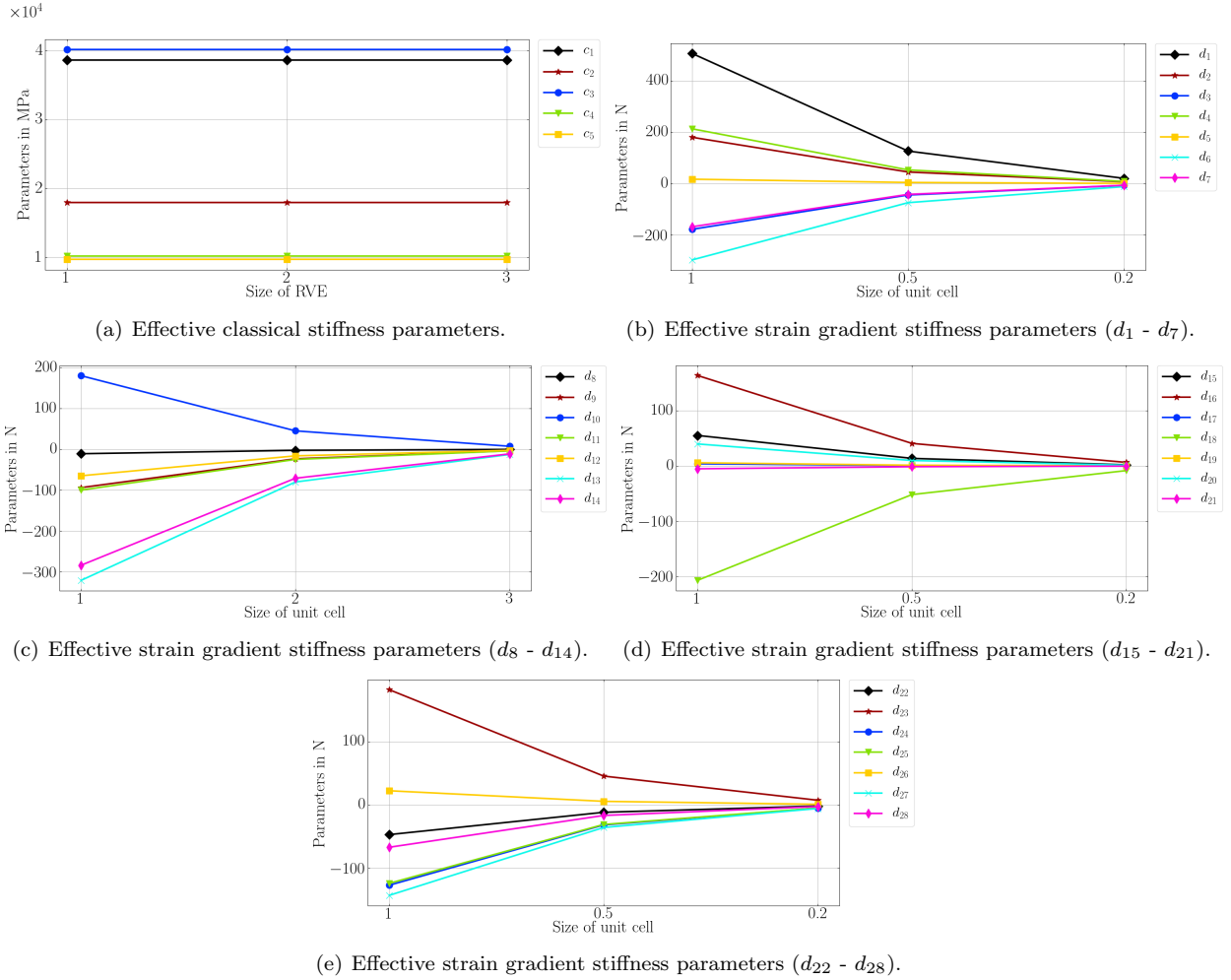


Figure 12: Effective material parameters with the changing lengths of unit cells, we emphasize that the sub-structure remains the same.

### 4.3.2 SiC/Al Metal Matrix Composite (MMC)

Aluminum-based MMCs have gained interest in engineering over the past three decades. The insertion of a ceramic material into an aluminum matrix leads to high stiffness and toughness of the composite material. In this section, the effective properties of SiC/Al metal matrix composite are investigated. RVE models have been



created for three-dimensional spherical particles embedded into the metal matrix. Filler is used as a reinforcement. Their volume ratios within the MMC vary from 0% to 38.2 % by volume. The material parameters taken from [46] are compiled in Table 8.

Table 8: Material properties used for SiC/Al metal matrix composite material.  $E$  Young's modulus,  $\nu$  Poisson's ratio, and  $\rho$  density.

Type	$E$ in GPa	$\nu$	$\rho$ in kg/m <sup>3</sup>
Matrix (Al2618-T4)	70	0.3	2900
Inclusion (SiC)	450	0.17	3100

The identified parameters for 61.8% volume ratio of matrix are found as follows

$$C_{AB}^M = \begin{pmatrix} 163.3 & 50.5 & 50.5 & 0.0 & 0.0 & 0.0 \\ 50.5 & 163.5 & 50.5 & 0.0 & 0.0 & 0.0 \\ 50.5 & 50.5 & 163.6 & 0.0 & 0.0 & 0.0 \\ 0.0 & 0.0 & 0.0 & 46.4 & 0.0 & 0.0 \\ 0.0 & 0.0 & 0.0 & 0.0 & 46.3 & 0.0 \\ 0.0 & 0.0 & 0.0 & 0.0 & 0.0 & 46.3 \end{pmatrix} \text{ GPa},$$

$$D_{\alpha\beta}^M = \begin{pmatrix} 7120.6 & 1075.0 & -844.4 & 1077.8 & -836.6 & 0.0 & 0.0 & 0.0 & 0.0 & 0.0 & 0.0 & 0.0 & 0.0 & 0.0 & 0.0 & 0.0 & 0.0 & 0.0 \\ 1075.0 & -2517.5 & -788.5 & -48.3 & -275.8 & 0.0 & 0.0 & 0.0 & 0.0 & 0.0 & 0.0 & 0.0 & 0.0 & 0.0 & 0.0 & 0.0 & 0.0 & 0.0 \\ -844.4 & -788.5 & 1914.3 & -276.5 & -347.3 & 0.0 & 0.0 & 0.0 & 0.0 & 0.0 & 0.0 & 0.0 & 0.0 & 0.0 & 0.0 & 0.0 & 0.0 & 0.0 \\ 1077.8 & -48.3 & -276.5 & -2515.1 & -789.7 & 0.0 & 0.0 & 0.0 & 0.0 & 0.0 & 0.0 & 0.0 & 0.0 & 0.0 & 0.0 & 0.0 & 0.0 & 0.0 \\ -836.6 & -275.8 & -347.3 & -789.7 & 1915.1 & 0.0 & 0.0 & 0.0 & 0.0 & 0.0 & 0.0 & 0.0 & 0.0 & 0.0 & 0.0 & 0.0 & 0.0 & 0.0 \\ 0.0 & 0.0 & 0.0 & 0.0 & 0.0 & 7130.6 & 1070.6 & -850.1 & 1076.5 & -840.1 & 0.0 & 0.0 & 0.0 & 0.0 & 0.0 & 0.0 & 0.0 & 0.0 \\ 0.0 & 0.0 & 0.0 & 0.0 & 0.0 & 1070.6 & -2504.4 & -781.2 & -48.1 & -276.2 & 0.0 & 0.0 & 0.0 & 0.0 & 0.0 & 0.0 & 0.0 & 0.0 \\ 0.0 & 0.0 & 0.0 & 0.0 & 0.0 & -850.1 & -781.2 & 1915.4 & -275.8 & -347.6 & 0.0 & 0.0 & 0.0 & 0.0 & 0.0 & 0.0 & 0.0 & 0.0 \\ 0.0 & 0.0 & 0.0 & 0.0 & 0.0 & 1076.5 & -48.1 & -275.8 & -2513.8 & -790.7 & 0.0 & 0.0 & 0.0 & 0.0 & 0.0 & 0.0 & 0.0 & 0.0 \\ 0.0 & 0.0 & 0.0 & 0.0 & 0.0 & -840.1 & -276.2 & -347.6 & -790.8 & 1917.1 & 0.0 & 0.0 & 0.0 & 0.0 & 0.0 & 0.0 & 0.0 & 0.0 \\ 0.0 & 0.0 & 0.0 & 0.0 & 0.0 & 0.0 & 0.0 & 0.0 & 0.0 & 0.0 & 7141.0 & 1072.0 & -848.8 & 1072.0 & -849.8 & 0.0 & 0.0 & 0.0 \\ 0.0 & 0.0 & 0.0 & 0.0 & 0.0 & 0.0 & 0.0 & 0.0 & 0.0 & 0.0 & 1072.0 & -2490.1 & -783.5 & -47.5 & -276.5 & 0.0 & 0.0 & 0.0 \\ 0.0 & 0.0 & 0.0 & 0.0 & 0.0 & 0.0 & 0.0 & 0.0 & 0.0 & 0.0 & -848.8 & -783.5 & 1915.3 & -275.4 & -350.4 & 0.0 & 0.0 & 0.0 \\ 0.0 & 0.0 & 0.0 & 0.0 & 0.0 & 0.0 & 0.0 & 0.0 & 0.0 & 0.0 & 1072.0 & -47.5 & -275.4 & -2506.2 & -786.2 & 0.0 & 0.0 & 0.0 \\ 0.0 & 0.0 & 0.0 & 0.0 & 0.0 & 0.0 & 0.0 & 0.0 & 0.0 & 0.0 & -849.8 & -276.5 & -350.4 & -786.2 & 1915.4 & 0.0 & 0.0 & 0.0 \\ 0.0 & 0.0 & 0.0 & 0.0 & 0.0 & 0.0 & 0.0 & 0.0 & 0.0 & 0.0 & 0.0 & 0.0 & 0.0 & 0.0 & 0.0 & -596.3 & -711.0 & -709.6 \\ 0.0 & 0.0 & 0.0 & 0.0 & 0.0 & 0.0 & 0.0 & 0.0 & 0.0 & 0.0 & 0.0 & 0.0 & 0.0 & 0.0 & 0.0 & -711.0 & -593.9 & -708.1 \\ 0.0 & 0.0 & 0.0 & 0.0 & 0.0 & 0.0 & 0.0 & 0.0 & 0.0 & 0.0 & 0.0 & 0.0 & 0.0 & 0.0 & 0.0 & -709.6 & -708.1 & -589.7 \end{pmatrix} \text{ N}.$$

Effected by the cubic material symmetry of the RVE, there are three independent parameters in the classical stiffness tensor,

$$C_{AB}^M = \begin{pmatrix} c_1 & c_2 & c_2 & 0 & 0 & 0 \\ c_2 & c_1 & c_2 & 0 & 0 & 0 \\ c_2 & c_2 & c_1 & 0 & 0 & 0 \\ 0 & 0 & 0 & c_3 & 0 & 0 \\ 0 & 0 & 0 & 0 & c_3 & 0 \\ 0 & 0 & 0 & 0 & 0 & c_3 \end{pmatrix}.$$

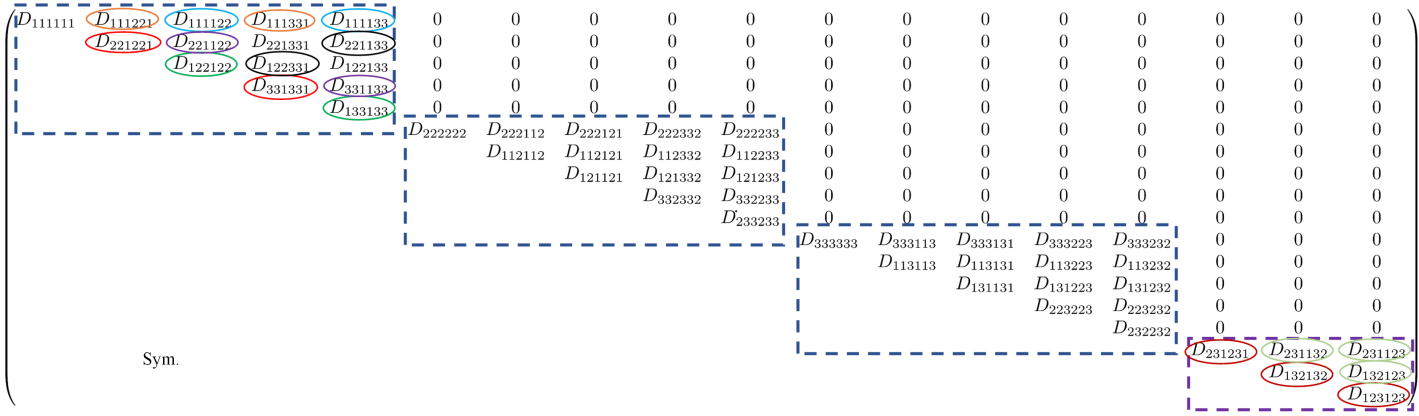


Figure 13: The structure of the strain gradient stiffness tensor for cubic materials. Three  $5 \times 5$  matrices in the diagonal are equal, For example,  $D_{111111} = D_{222222}$ . In the first  $5 \times 5$  matrix, it is also observed that  $D_{111221} = D_{111331}$ ,  $D_{111122} = D_{111133}$ ,  $D_{221221} = D_{331331}$ ,  $D_{122122} = D_{133133}$ ,  $D_{221122} = D_{331133}$ ,  $D_{221133} = D_{122331}$ . In the  $3 \times 3$  matrix,  $D_{231231} = D_{132132} = D_{123123}$ ,  $D_{231132} = D_{231123} = D_{132123}$ .

As shown in Figure 13, excluding the parameters of the same value, there are 11 parameters found in the strain gradient stiffness tensor,

$$\begin{pmatrix}
 d_1 & d_2 & d_3 & d_2 & d_3 & 0 & 0 & 0 & 0 & 0 & 0 & 0 & 0 & 0 & 0 & 0 & 0 & 0 & 0 \\
 & d_4 & d_5 & d_6 & d_7 & 0 & 0 & 0 & 0 & 0 & 0 & 0 & 0 & 0 & 0 & 0 & 0 & 0 & 0 \\
 & & d_8 & d_7 & d_9 & 0 & 0 & 0 & 0 & 0 & 0 & 0 & 0 & 0 & 0 & 0 & 0 & 0 & 0 \\
 & & & d_4 & d_5 & 0 & 0 & 0 & 0 & 0 & 0 & 0 & 0 & 0 & 0 & 0 & 0 & 0 & 0 \\
 & & & & d_8 & 0 & 0 & 0 & 0 & 0 & 0 & 0 & 0 & 0 & 0 & 0 & 0 & 0 & 0 \\
 & & & & & d_1 & d_2 & d_3 & d_2 & d_3 & 0 & 0 & 0 & 0 & 0 & 0 & 0 & 0 & 0 \\
 & & & & & & d_4 & d_5 & d_6 & d_7 & 0 & 0 & 0 & 0 & 0 & 0 & 0 & 0 & 0 \\
 & & & & & & & d_8 & d_7 & d_9 & 0 & 0 & 0 & 0 & 0 & 0 & 0 & 0 & 0 \\
 & & & & & & & & d_4 & d_5 & 0 & 0 & 0 & 0 & 0 & 0 & 0 & 0 & 0 \\
 & & & & & & & & & d_8 & 0 & 0 & 0 & 0 & 0 & 0 & 0 & 0 & 0 \\
 & & & & & & & & & & d_1 & d_2 & d_3 & d_2 & d_3 & 0 & 0 & 0 & 0 \\
 & & & & & & & & & & & d_4 & d_5 & d_6 & d_7 & 0 & 0 & 0 & 0 \\
 & & & & & & & & & & & & d_8 & d_7 & d_9 & 0 & 0 & 0 & 0 \\
 & & & & & & & & & & & & & d_4 & d_5 & 0 & 0 & 0 & 0 \\
 & & & & & & & & & & & & & & d_8 & 0 & 0 & 0 & 0 \\
 & & & & & & & & & & & & & & & d_{10} & d_{11} & d_{11} & \\
 & & & & & & & & & & & & & & & & d_{10} & d_{11} & \\
 & & & & & & & & & & & & & & & & & d_{10} & \\
 & & & & & & & & & & & & & & & & & & d_{10}
 \end{pmatrix}$$

Please note, among these 11 parameters, some of them might be linearly dependent. Further investigations are conducted for different volume fraction of matrix, different sizes of selected RVE, and different sizes of unit cells as indicated in Figures 14, 16, 18. Results are displayed in Figures 15, 17, 19. It is observed that the higher order parameters are zero when materials are homogeneous; they are independent of the stack of RVEs, and they are sensitive to microstructural sizes as well as following the scaling rule.

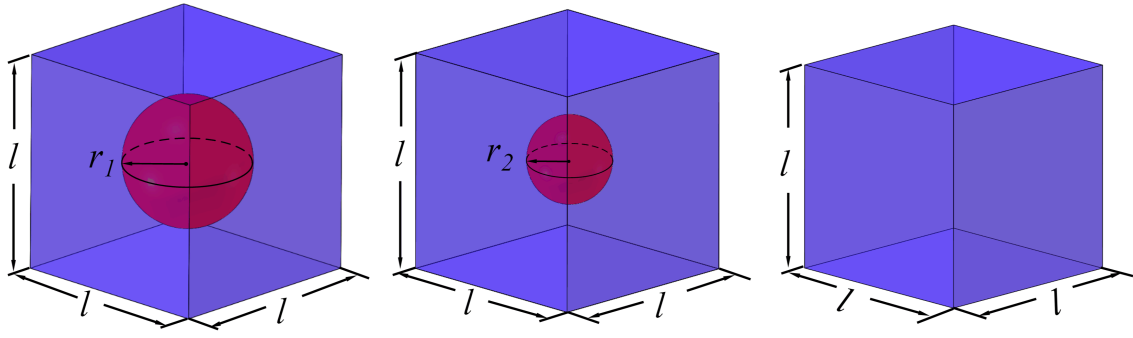


Figure 14: Changing volume fraction of matrix.

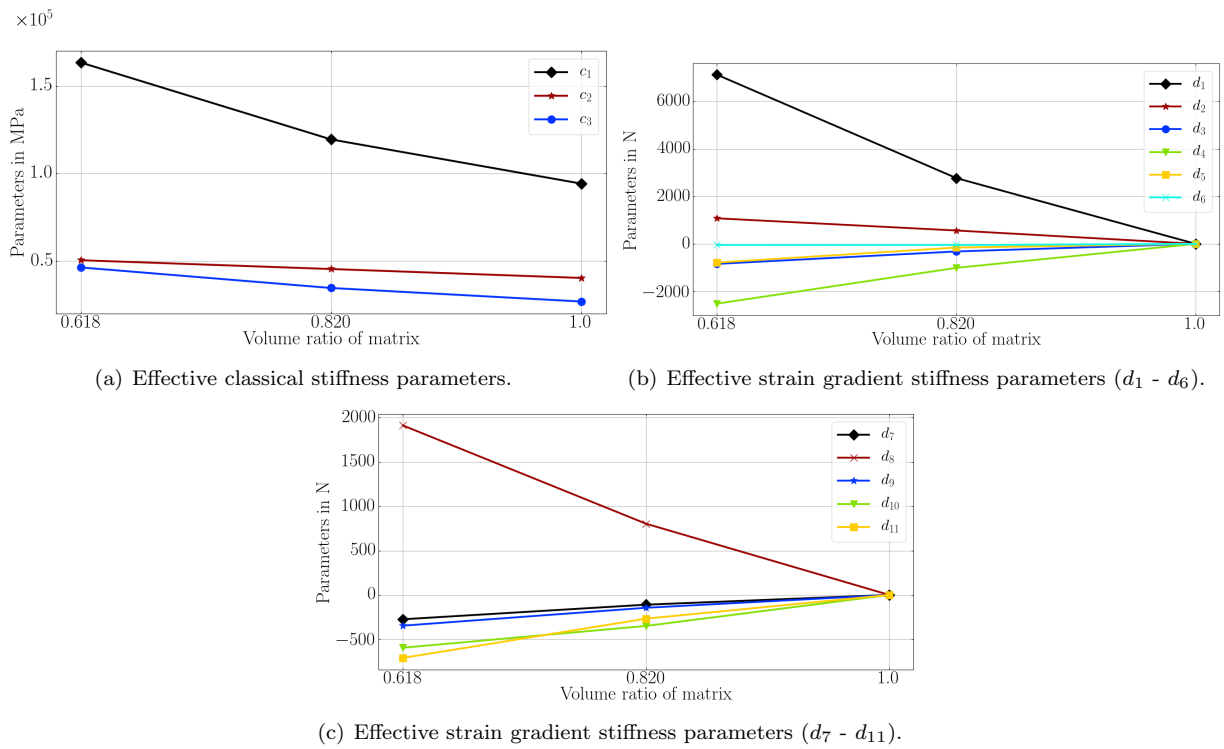


Figure 15: Effective material parameters with the changing of volume fraction of matrix.

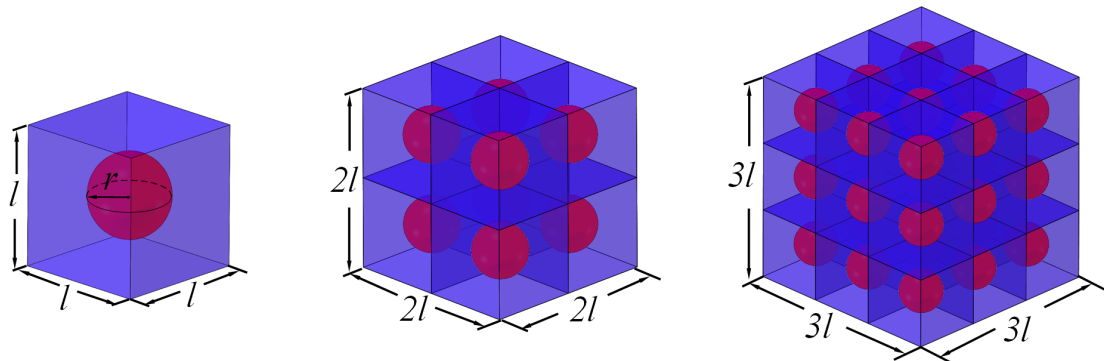


Figure 16: RVEs constructed by 1 unit cell, 8 unit cells, 27 unit cells.

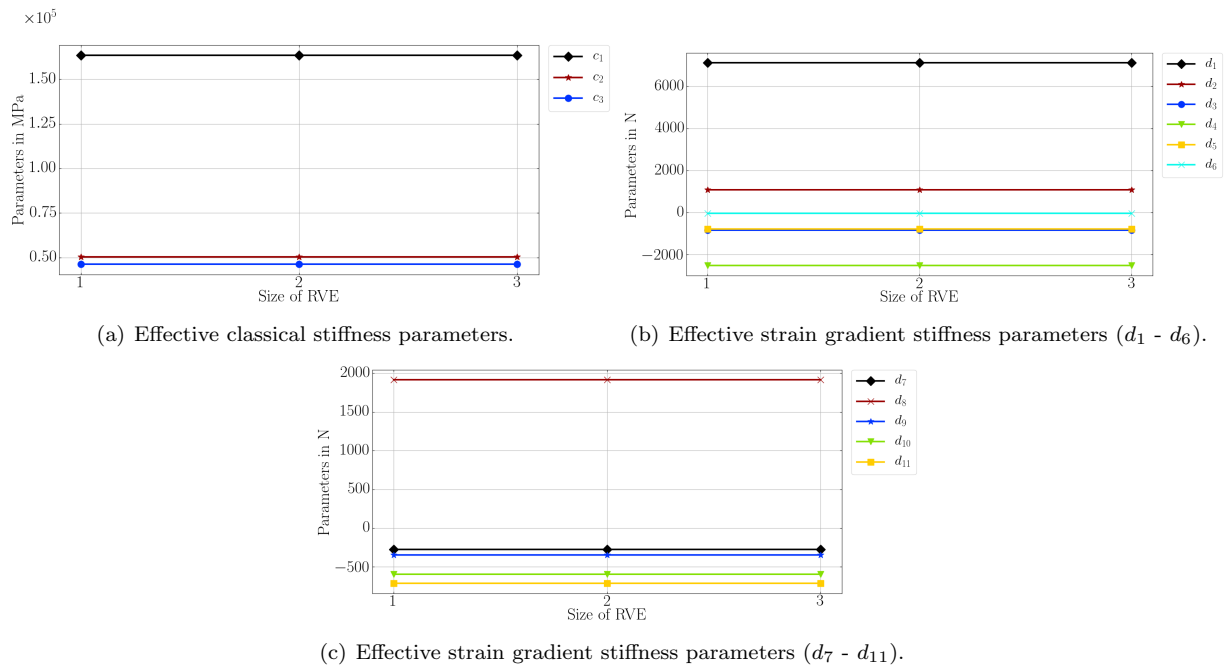


Figure 17: Effective material parameters with the changing RVE sizes ( $1 \times 1 \times 1$ ,  $2 \times 2 \times 2$ ,  $3 \times 3 \times 3$ ).

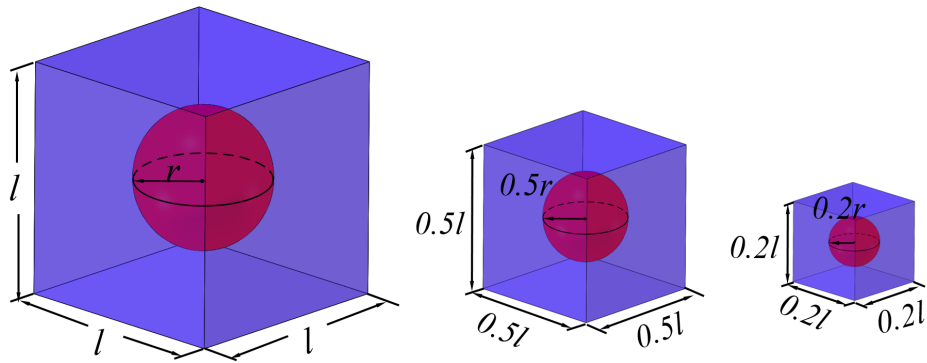


Figure 18: Unit cells with changing lengths.

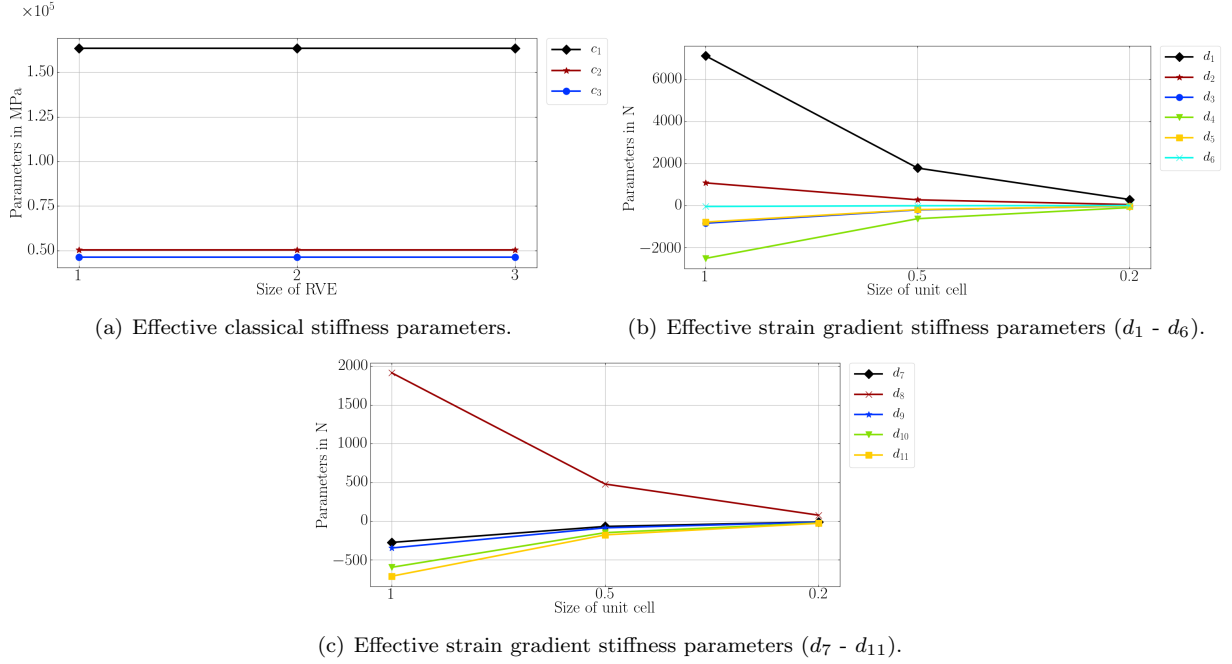


Figure 19: Effective material parameters with the changing lengths of unit cells.

### 4.3.3 Aluminum foam

Aluminum foam is a highly porous metallic material with a cellular substructure. The RVEs of the aluminum foam are modeled by using a cubic inclusion, which are literally voids embedded in a matrix made of aluminum. In order to avoid numerical problems, a small number is assigned to the Young's modulus of voids. Indeed, this benchmark case is challenging to obtain consistently by using other procedures in the literature, where the mass density in the microscale is exchanged with the volume averaged mass density. The parameters do not show a monotonous convergence. Herein, the change in the formulation solves the problem by considering a distinction between mass densities leading to correct results in  $\psi$  and thus in  $\mathbf{G}$  and  $\mathbf{D}$  parameters. The material properties used for aluminum foam is found in Table 9.

Table 9: Material properties used for aluminum foam.  $E$  Young's modulus,  $\nu$  Poisson's ratio, and  $\rho$  mass density.

Type	$E$ in GPa	$\nu$	$\rho$ in $\text{kg/m}^3$
Matrix (Aluminum)	70	0.3	2700
Inclusion (Voids)	$10^{-10}$	0.0	0.0

The identified parameters are found as follows:

$$C_{AB}^M = \begin{pmatrix} 15.1 & 3.0 & 3.0 & 0.0 & 0.0 & 0.0 \\ 3.0 & 15.1 & 3.0 & 0.0 & 0.0 & 0.0 \\ 3.0 & 3.0 & 15.1 & 0.0 & 0.0 & 0.0 \\ 0.0 & 0.0 & 0.0 & 2.9 & 0.0 & 0.0 \\ 0.0 & 0.0 & 0.0 & 0.0 & 2.9 & 0.0 \\ 0.0 & 0.0 & 0.0 & 0.0 & 0.0 & 2.9 \end{pmatrix} \text{ GPa} ,$$

$$D_{\alpha\beta}^M = \begin{pmatrix} 1130.3 & 185.4 & 288.8 & 184.8 & 288.6 & 0.0 & 0.0 & 0.0 & 0.0 & 0.0 & 0.0 & 0.0 & 0.0 & 0.0 & 0.0 & 0.0 & 0.0 & 0.0 \\ 185.4 & 1080.6 & 114.9 & 328.0 & 74.6 & 0.0 & 0.0 & 0.0 & 0.0 & 0.0 & 0.0 & 0.0 & 0.0 & 0.0 & 0.0 & 0.0 & 0.0 & 0.0 \\ 288.8 & 114.9 & -42.8 & 74.5 & 160.7 & 0.0 & 0.0 & 0.0 & 0.0 & 0.0 & 0.0 & 0.0 & 0.0 & 0.0 & 0.0 & 0.0 & 0.0 & 0.0 \\ 184.8 & 328.0 & 74.5 & 1080.3 & 114.9 & 0.0 & 0.0 & 0.0 & 0.0 & 0.0 & 0.0 & 0.0 & 0.0 & 0.0 & 0.0 & 0.0 & 0.0 & 0.0 \\ 288.6 & 74.6 & 160.7 & 114.9 & -42.6 & 0.0 & 0.0 & 0.0 & 0.0 & 0.0 & 0.0 & 0.0 & 0.0 & 0.0 & 0.0 & 0.0 & 0.0 & 0.0 \\ 0.0 & 0.0 & 0.0 & 0.0 & 0.0 & 1139.1 & 187.6 & 290.6 & 186.9 & 290.2 & 0.0 & 0.0 & 0.0 & 0.0 & 0.0 & 0.0 & 0.0 & 0.0 \\ 0.0 & 0.0 & 0.0 & 0.0 & 0.0 & 187.6 & 1081.0 & 114.7 & 328.4 & 75.0 & 0.0 & 0.0 & 0.0 & 0.0 & 0.0 & 0.0 & 0.0 & 0.0 \\ 0.0 & 0.0 & 0.0 & 0.0 & 0.0 & 290.6 & 114.7 & -42.8 & 74.9 & 161.0 & 0.0 & 0.0 & 0.0 & 0.0 & 0.0 & 0.0 & 0.0 & 0.0 \\ 0.0 & 0.0 & 0.0 & 0.0 & 0.0 & 186.9 & 328.4 & 74.9 & 1080.4 & 115.4 & 0.0 & 0.0 & 0.0 & 0.0 & 0.0 & 0.0 & 0.0 & 0.0 \\ 0.0 & 0.0 & 0.0 & 0.0 & 0.0 & 290.2 & 75.0 & 161.0 & 115.4 & -42.5 & 0.0 & 0.0 & 0.0 & 0.0 & 0.0 & 0.0 & 0.0 & 0.0 \\ 0.0 & 0.0 & 0.0 & 0.0 & 0.0 & 0.0 & 0.0 & 0.0 & 0.0 & 1171.8 & 194.3 & 296.5 & 194.5 & 296.9 & 0.0 & 0.0 & 0.0 & 0.0 \\ 0.0 & 0.0 & 0.0 & 0.0 & 0.0 & 0.0 & 0.0 & 0.0 & 0.0 & 194.3 & 1082.3 & 115.6 & 329.8 & 76.3 & 0.0 & 0.0 & 0.0 & 0.0 \\ 0.0 & 0.0 & 0.0 & 0.0 & 0.0 & 0.0 & 0.0 & 0.0 & 0.0 & 296.5 & 115.6 & -42.1 & 76.3 & 162.0 & 0.0 & 0.0 & 0.0 & 0.0 \\ 0.0 & 0.0 & 0.0 & 0.0 & 0.0 & 0.0 & 0.0 & 0.0 & 0.0 & 194.5 & 329.8 & 76.3 & 1082.1 & 115.8 & 0.0 & 0.0 & 0.0 & 0.0 \\ 0.0 & 0.0 & 0.0 & 0.0 & 0.0 & 0.0 & 0.0 & 0.0 & 0.0 & 296.9 & 76.3 & 162.0 & 115.8 & -42.0 & 0.0 & 0.0 & 0.0 & 0.0 \\ 0.0 & 0.0 & 0.0 & 0.0 & 0.0 & 0.0 & 0.0 & 0.0 & 0.0 & 0.0 & 0.0 & 0.0 & 0.0 & 0.0 & 406.8 & 19.6 & 19.9 & 0.0 \\ 0.0 & 0.0 & 0.0 & 0.0 & 0.0 & 0.0 & 0.0 & 0.0 & 0.0 & 0.0 & 0.0 & 0.0 & 0.0 & 0.0 & 19.6 & 406.7 & 19.8 & 0.0 \\ 0.0 & 0.0 & 0.0 & 0.0 & 0.0 & 0.0 & 0.0 & 0.0 & 0.0 & 0.0 & 0.0 & 0.0 & 0.0 & 0.0 & 19.9 & 19.8 & 406.9 & 0.0 \end{pmatrix} \text{N}.$$

Three independent parameters and eleven parameters are observed in the classical stiffness tensor and the strain gradient stiffness tensor, respectively. This is consistent to the cubic material symmetry as mentioned before. Investigations on the different volume fraction of matrix, repetition of RVEs, changing sizes of unit cells are conducted as displayed in Figures 20, 22, 24. Corresponding outcomes are presented in Figures 21, 23, 25.

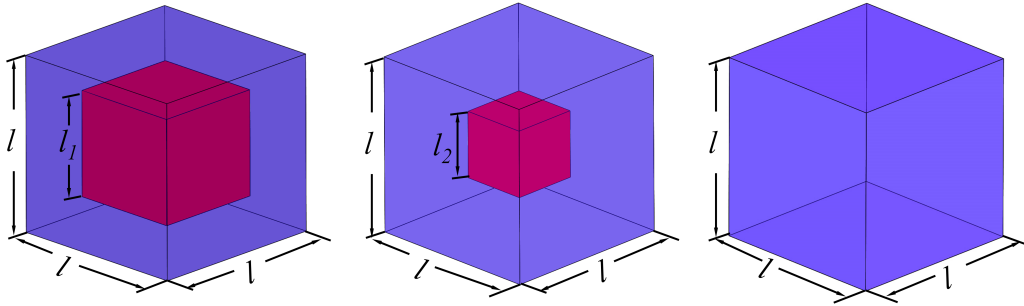


Figure 20: Different volume fraction of matrix for the aluminum foam.

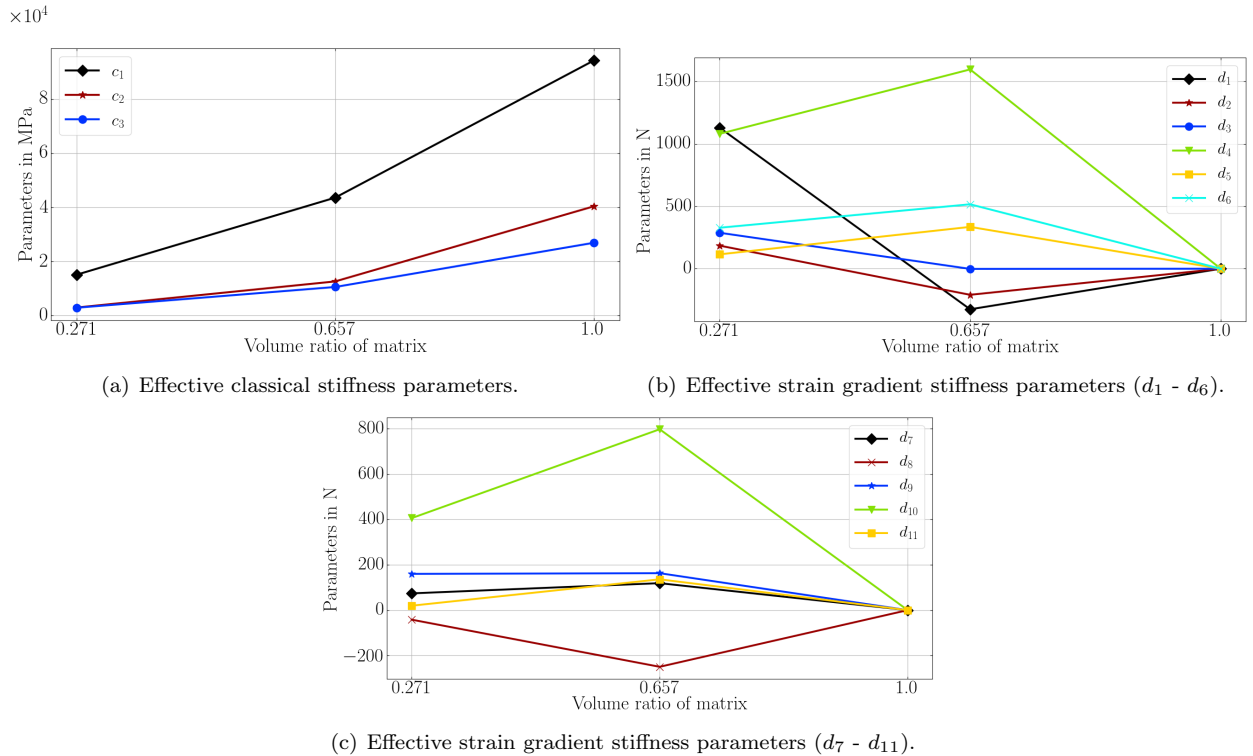


Figure 21: Effective material parameters with changing of volume fraction of matrix.

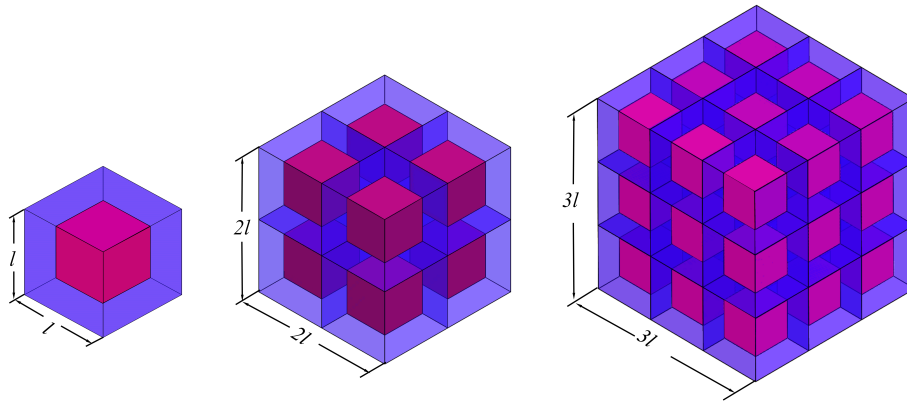


Figure 22: RVEs constructed by 1 unit cell, 8 unit cells, 27 unit cells.

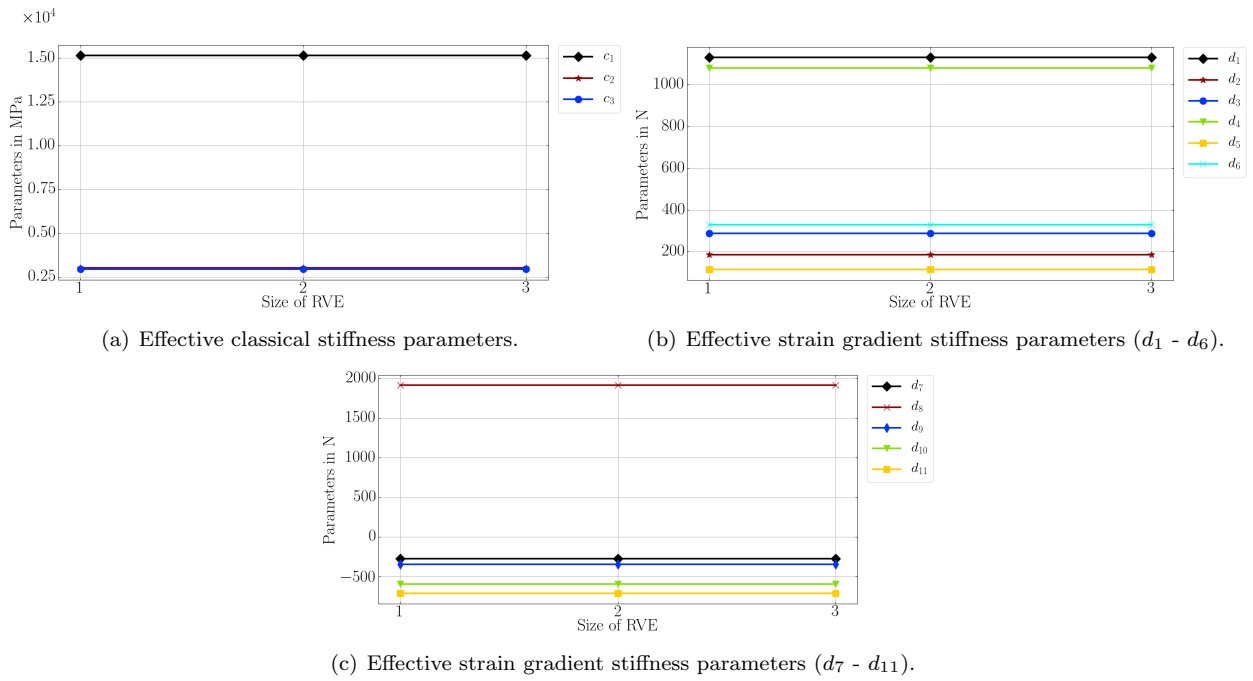


Figure 23: Effective material parameters with changing RVE sizes ( $1 \times 1 \times 1$ ,  $2 \times 2 \times 2$ ,  $3 \times 3 \times 3$ ).

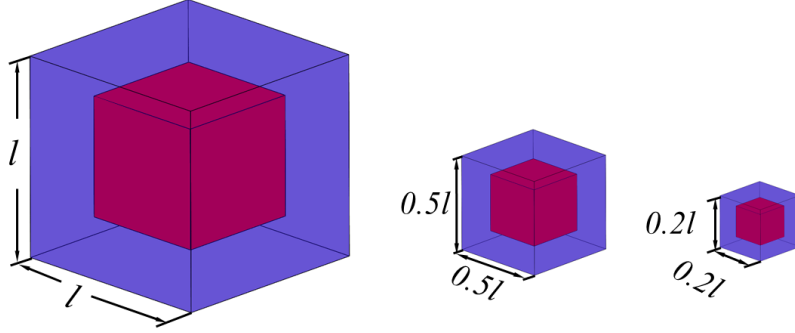


Figure 24: Unit cells with changing lengths.

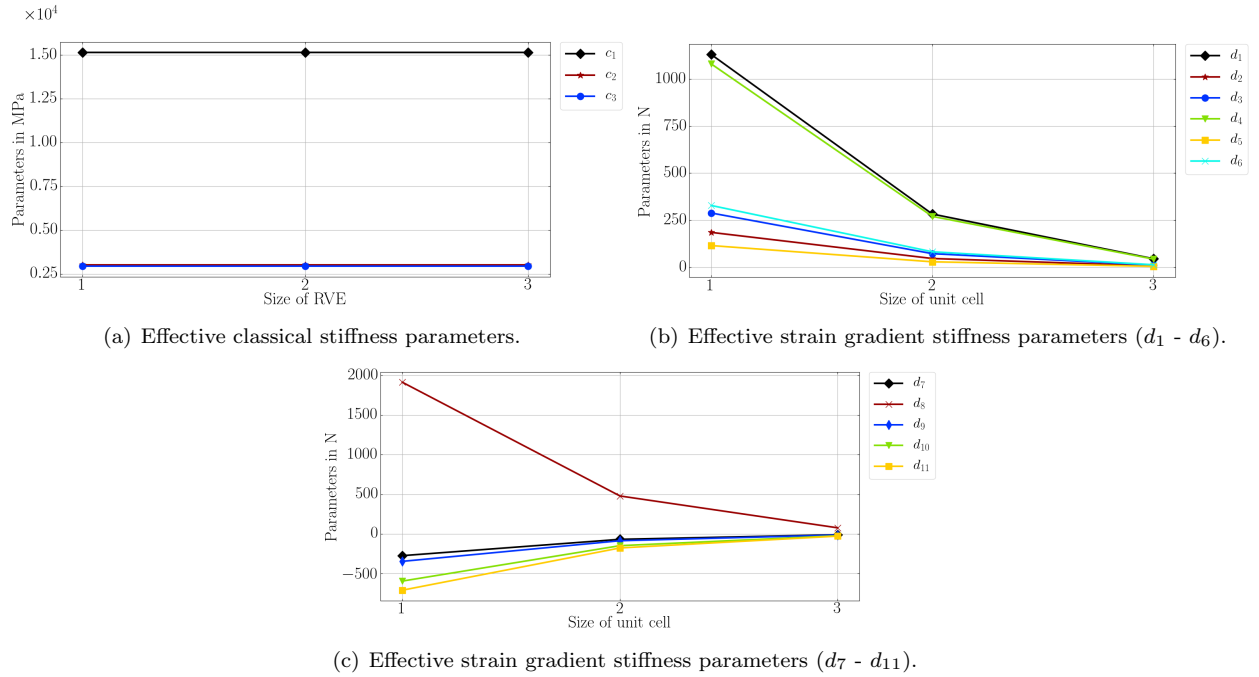


Figure 25: Effective material parameters with changing lengths of unit cells.

## 5 Remark on positive definiteness

As observed from the previous sections, negative values appear in strain gradient stiffness tensors. This fact may raise concerns regarding the positive definiteness of the strain energy function. In [9, 47, 48, 49], the issue of positive definiteness of the strain energy function for strain gradient materials is addressed and bounds on material parameters are provided. The bounds on strain gradient constants consider the continuum to be purely local, which means that the strain energy function is convex with respect to every material point [9]. However, when homogenizing the microstructures of composite materials with an equivalent strain gradient continuum, we have a limited non-locality. The non-locality originates from the energy equivalence as shown in Eqn. (1). We emphasize that the  $\epsilon$  is a finite number,  $\epsilon < 1$  but not necessarily  $\epsilon \ll 1$ , which means that the studied composite material has a finite macroscopic and microscopic sizes. Therefore, the strain energy function averaged over this microstructure size should be positive definite and not the pointwise local strain



energy function. Thus coefficients in the strain gradient stiffness tensor could be negative as long as the strain energy density function integrated over the periodic unit cell is positive definite. This interpretation is aligned with in [12, 36, 35]. Additionally, this condition is always fulfilled if the microstructure energy density is positive definite, since Eqn. (1) is enforced.

## 6 Verification of the homogenized strain gradient models

In order to assess the homogenized strain gradient continuum model developed in this paper, finite element computations are conducted to evaluate the performance of the proposed model. To this end, a cantilever beam bending problem is selected as presented in Figure 26. The beam is made out of aluminum foam with periodically aligned microstructures of  $1 \text{ mm} \times 1 \text{ mm} \times 1 \text{ mm}$ . As mentioned above, the inclusions of the microstructures are voids. We use the determined parameters with matrix volume fraction of 0.271 as shown in Figure 21. The length, width, and height of the beam are assigned to be 50 mm, 2 mm, and 2 mm. The left surface,  $X_1 = 0$ , of the beam is clamped ( $u_1 = u_2 = u_3 = 0$ ). A traction is applied at the right surface  $X_1 = L$ .

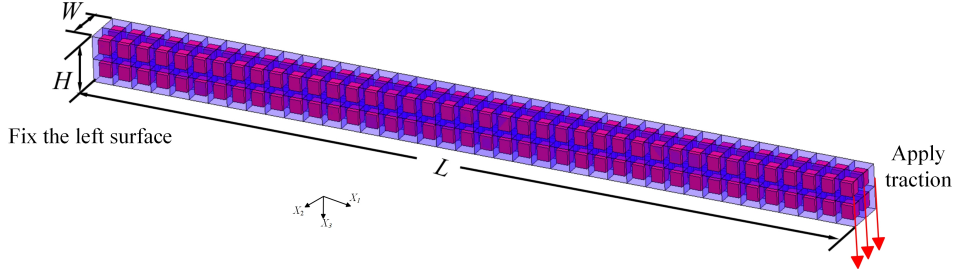


Figure 26: Schematic of a cantilever beam bending problem. The length, width, and height of the beam is  $L$ ,  $W$ ,  $H$ . The inclusions (voids) are presented as red and matrix is indicated as blue (with less opacity for the sake of visualization).

We conduct three simulations. A Direct Numerical Simulation (DNS), where the microstructure is modeled in detail. This result is accepted as correct. A homogenization simulation with second order (strain gradient) theory, where  $\mathbf{D}$  and  $\mathbf{G}$  tensors are employed. A homogenized simulation with first order theory, in other words,  $\mathbf{D}$  and  $\mathbf{G}$  are set to zero (first order theory is used). As  $C^1$  continuity is required for the numerical implementation of the strain gradient computations, the isogeometric analysis is used in the simulations for the homogenized models. The codes developed and verified in [50] are used herein. The weak form for linear elastic strain gradient materials is presented as

$$\int_{\Omega} \left( \sigma_{ij} \delta u_{i,j} + \tau_{ijk} \delta u_{i,jk} \right) dV = \int_{\partial\Omega} t_i \delta u_i dA, \quad (30)$$

where  $\sigma_{ij}$  and  $\tau_{ijk}$  are the stress tensor and hyperstress tensor defined by

$$\sigma_{ij} = \frac{\partial w^M}{\partial u_{i,j}}, \quad \tau_{ijk} = \frac{\partial w^M}{\partial u_{i,jk}}. \quad (31)$$

with  $w$  the strain energy density. The body forces, double traction, and the so-called wedge forces are all set to be zero, therefore the pertinent terms in the weak form Eqn. (30) are neglected. The traction is applied incrementally from  $(0, 0, 0)$  to  $(0, 0, 0.001 \text{ MPa})$ . The calculated results of total displacement are shown in Figure 27. Strain gradient results match accurately DNS results. However, a significant deviation from DNS is observed, if one uses first order theory. DNS shows that the beam "act" stiffer than first order theory suggests, this experimentally well known fact is called size effect. The difference vanishes as homothetic ratio approaches zero, in other words, the same foam in a larger beam shows no size effect. Such phenomenon is also observed in the numerical investigation in [51, 52] In order to assess the models further, more investigations are made as displayed in Figure 28 and Figure 29.

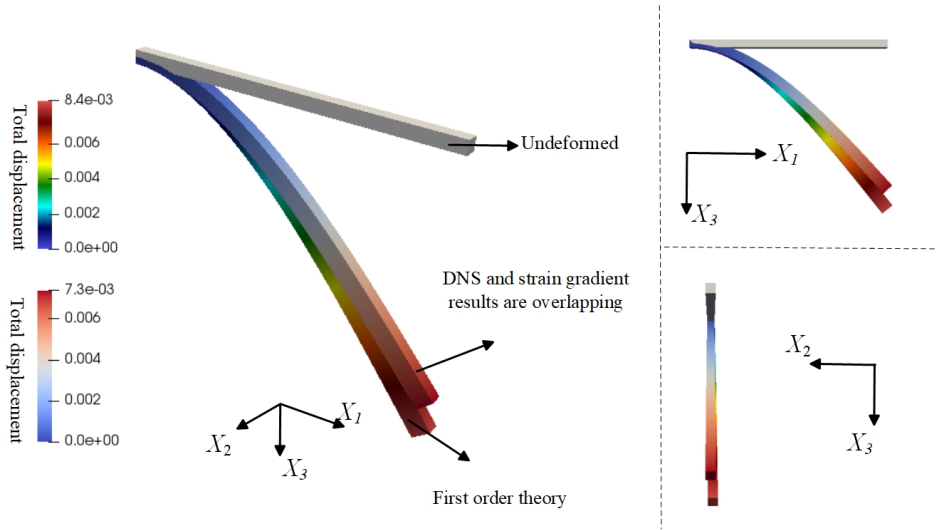


Figure 27: Comparisons of total displacement among the heterogeneous Cauchy continuum, homogenized strain gradient continuum, and the homogenized Cauchy continuum in the case of cantilever beam bending. Scaling factor 5000.

The elapsed time for DNS is 771.5 s by using a computer (Intel(R) Core(TM) i7-8565U CPU). The elapsed time for the homogenized Cauchy model and the strain gradient model is 15.0 s and 59.7 s as shown in Figure 28(a). It is evident that by using the homogenization techniques, computational efficiency is greatly improved. Additional difficulty is the challenge for the meshing algorithm to construct a high quality mesh for the microstructure. Element quality will not be ensured around sharp edges leading to inconsistencies as well as strain concentrations making the model error-prone. On the other hand, a homogeneous structure faces only macroscopic sharp contours such that a mesh convergence is feasible to minimize the numerical errors. Indeed, the computational efficiency of the first order theory is significantly larger than the second order theory, even in the same type of mesh. But for the chosen homothetic ratio herein, we obtain an inadequate result from the first order theory as indicated in Figure 28(b) and Figure 29.

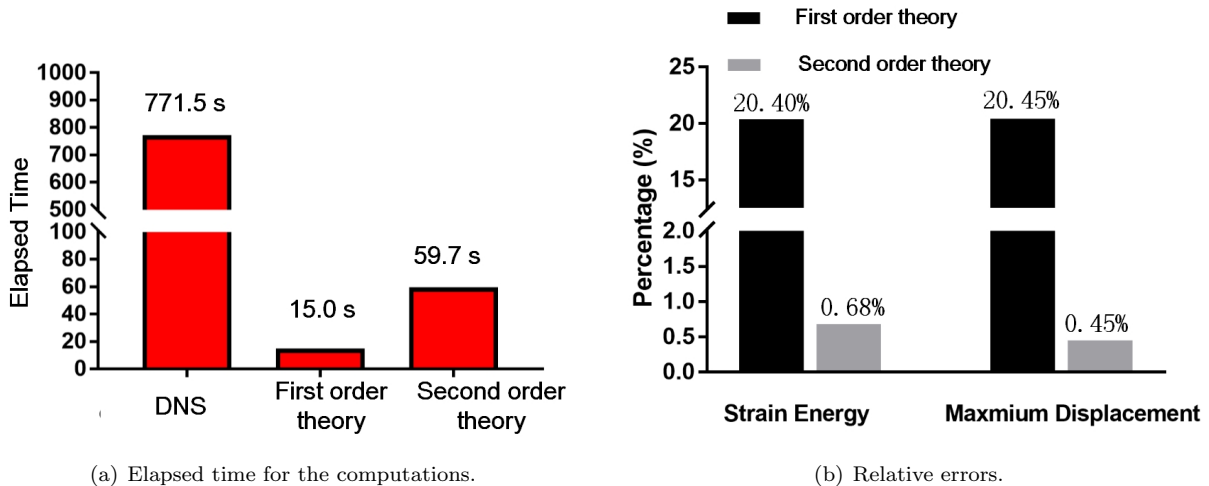


Figure 28: Comparisons of the elapsed time, the relative errors of the strain energy and maximum displacement for the first order theory and second order theory results.

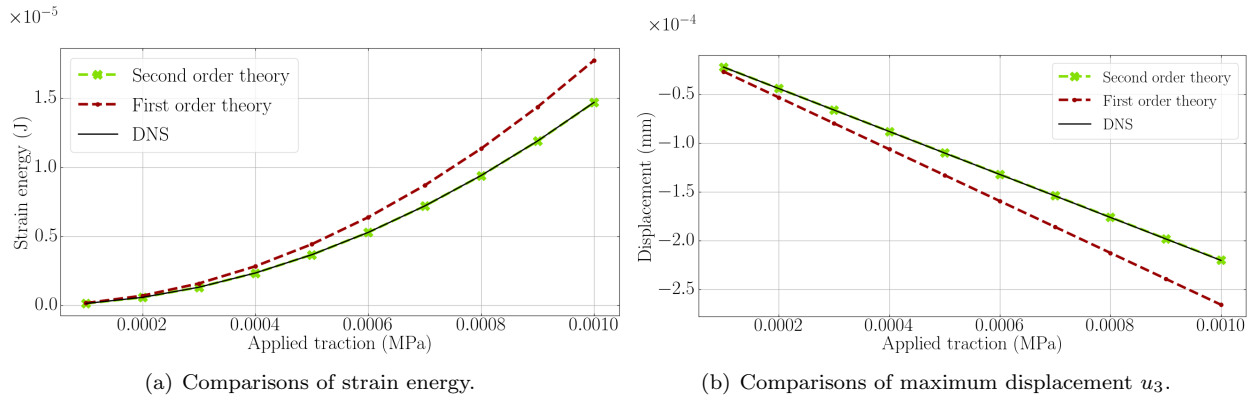


Figure 29: Comparisons of the calculated strain energy and maximum displacement among DNS, first order theory, and second order theory results.

## 7 Conclusions

Asymptotic homogenization method has been employed to homogenize composite material into effective homogeneous strain gradient continua. Main conclusions are summarized as follows:

- Purely computational analysis determines all the parameters in the strain gradient theory. In particular, the parameters in the rank five tensor and the rank six tensor.
- Numerical examples for 2D and 3D, stiff and soft inclusions, cubic and transverse material symmetry cases have been conducted.
- In both 2D and 3D numerical examples, the effective strain gradient parameters vanish when materials are purely homogeneous, they are independent of repetitions of RVEs and sensitive to microstructural sizes.
- Without assuming a specific symmetry group, in the case of cubic symmetry, all expected relations have been captured by the proposed formalism.
- Physical meaning of the homothetic ratio  $\epsilon$  is interpreted, a so-called scaling rule for effective strain gradient parameters has been discussed. The method is valid when  $\epsilon$  is a finite value.  $\epsilon < 1$  is required but not necessarily  $\epsilon \ll 1$ .
- An evaluation of the performance of the determined strain gradient parameters is done in 3D for the first time. It is found that including the strain gradient terms in the homogenized model will improve the accuracy of the prediction of the response of aluminum foams compared to classical (first order) homogenization.

The homogenization tool is applicable to any composite materials with a periodic substructure at the microscale. Such multiscale are nowadays possible to manufacture by 3D printers. Therefore, effective parameters determination is of interest for a possible topology optimization. Further investigations will focus on the following aspects:

- To validate the identified parameters not only in statics but also in vibration responses, buckling critical loads [53], and wave propagation [54, 55].
- To apply the homogenization method to the analysis of 3D composite materials with finite thickness. This may be achieved by modeling the full thickness unit cell model and relieving the out-of-plane periodicity of the unit cell [56].
- To explore the possibility of studying more sophisticated metamaterials such as the so-called pantographic structures [29, 30] or the biomimetic spinodoids metamaterials [57] by the homogenization method.
- To extend the homogenization method to non-linear regime [58, 59] and multiphysics fields.

## References

- [1] Claude Boutin.  
Microstructural effects in elastic composites.  
*International Journal of Solids and Structures*, 33(7):1023–1051, 1996.
- [2] Justin Dirrenberger, Samuel Forest, and Dominique Jeulin.  
Computational homogenization of architected materials.  
In Yuri Estrin, Yves Bréchet, John Dunlop, and Peter” Fratzl, editors, *Architected materials in nature and engineering*, Springer Series in Materials Science, pages 89–139. Springer, 2019.
- [3] Sajad Arabnejad and Damiano Pasini.  
Mechanical properties of lattice materials via asymptotic homogenization and comparison with alternative homogenization methods.  
*International Journal of Mechanical Sciences*, 77:249–262, 2013.
- [4] Qiang Chen, George Chatzigeorgiou, and Fodil Meraghni.  
Extended mean-field homogenization of viscoelastic-viscoplastic polymer composites undergoing hybrid progressive degradation induced by interface debonding and matrix ductile damage.  
*International Journal of Solids and Structures*, 210:1–17, 2020.
- [5] J Yvonnet, Nicolas Auffray, and V Monchiet.  
Computational second-order homogenization of materials with effective anisotropic strain-gradient behavior.  
*International Journal of Solids and Structures*, 2020.
- [6] Lukáš Jakabčín and Pierre Seppecher.  
On periodic homogenization of highly contrasted elastic structures.  
*Journal of the Mechanics and Physics of Solids*, 144:104104, 2020.
- [7] Scott J Hollister and Noboru Kikuchi.  
A comparison of homogenization and standard mechanics analyses for periodic porous composites.  
*Computational mechanics*, 10(2):73–95, 1992.
- [8] Wolfgang H Müller.  
The experimental evidence for higher gradient theories.  
In A Bertram and S Forest, editors, *Mechanics of Strain Gradient Materials*, volume 600 of *CISM International Centre for Mechanical Sciences*, pages 1–18. Springer, 2020.
- [9] Raymond David Mindlin and NN Eshel.  
On first strain-gradient theories in linear elasticity.  
*International Journal of Solids and Structures*, 4(1):109–124, 1968.
- [10] A Cemal Eringen.  
Theory of micropolar elasticity.  
In *Microcontinuum field theories*, pages 101–248. Springer, 1999.
- [11] Holm Altenbach and Samuel Forest.  
*Generalized continua as models for classical and advanced materials*.  
Springer, 2016.
- [12] Rajesh S Kumar and David L McDowell.  
Generalized continuum modeling of 2-D periodic cellular solids.  
*International Journal of solids and structures*, 41(26):7399–7422, 2004.
- [13] F Dos Reis and JF Ganghoffer.  
Construction of micropolar continua from the asymptotic homogenization of beam lattices.  
*Computers & Structures*, 112:354–363, 2012.
- [14] Andrzej Skrzat and Victor A Eremeyev.  
On the effective properties of foams in the framework of the couple stress theory.  
*Continuum Mechanics and Thermodynamics*, pages 1–23, 2020.
- [15] Varvara Kouznetsova, Marc GD Geers, and WA Marcel Brekelmans.  
Multi-scale constitutive modelling of heterogeneous materials with a gradient-enhanced computational homogenization scheme.  
*International journal for numerical methods in engineering*, 54(8):1235–1260, 2002.

- [16] Ibrahim Goda and Jean-François Ganghoffer.  
Construction of first and second order grade anisotropic continuum media for 3d porous and textile composite structures.  
*Composite Structures*, 141:292–327, 2016.
- [17] Houssam Abdoul-Anziz, Pierre Seppecher, and Cédric Bellis.  
Homogenization of frame lattices leading to second gradient models coupling classical strain and strain-gradient terms.  
*Mathematics and Mechanics of Solids*, 24(12):3976–3999, 2019.
- [18] Oliver Weeger.  
Numerical homogenization of second gradient, linear elastic constitutive models for cubic 3d beam-lattice metamaterials.  
*International Journal of Solids and Structures*, 2021.
- [19] Samuel Forest and Duy Khanh Trinh.  
Generalized continua and non-homogeneous boundary conditions in homogenisation methods.  
*ZAMM-Journal of Applied Mathematics and Mechanics/Zeitschrift für Angewandte Mathematik und Mechanik*, 91(2):90–109, 2011.
- [20] Ondřej Rokoš, Maqsood M Ameen, Ron HJ Peerlings, and Mark GD Geers.  
Micromorphic computational homogenization for mechanical metamaterials with patterning fluctuation fields.  
*Journal of the Mechanics and Physics of Solids*, 123:119–137, 2019.
- [21] Shutian Liu and Wenzheng Su.  
Effective couple-stress continuum model of cellular solids and size effects analysis.  
*International Journal of Solids and Structures*, 46(14-15):2787–2799, 2009.
- [22] Victor A Eremeyev.  
On effective properties of materials at the nano-and microscales considering surface effects.  
*Acta Mechanica*, 227(1):29–42, 2016.
- [23] JF Ganghoffer and H Reda.  
A variational approach of homogenization of heterogeneous materials towards second gradient continua.  
*Mechanics of Materials*, page 103743, 2021.
- [24] Andrea Bacigalupo, Marco Paggi, F Dal Corso, and D Bigoni.  
Identification of higher-order continua equivalent to a Cauchy elastic composite.  
*Mechanics Research Communications*, 93:11–22, 2018.
- [25] Claude Boutin, Francesco dell’Isola, Ivan Giorgio, and Luca Placidi.  
Linear pantographic sheets: Asymptotic micro-macro models identification.  
*Mathematics and Mechanics of Complex Systems*, 5(2):127–162, 2017.
- [26] VG Kouznetsova, Marc GD Geers, and WAM1112 Brekelmans.  
Multi-scale second-order computational homogenization of multi-phase materials: a nested finite element solution strategy.  
*Computer methods in applied Mechanics and Engineering*, 193(48-51):5525–5550, 2004.
- [27] Giuseppe Rosi, Luca Placidi, and Nicolas Auffray.  
On the validity range of strain-gradient elasticity: a mixed static-dynamic identification procedure.  
*European Journal of Mechanics-A/Solids*, 69:179–191, 2018.
- [28] Giuseppe Rosi.  
Waves and generalized continua.  
In H Altenbach and A Öchsner, editors, *Encyclopedia of Continuum Mechanics*, pages 2756–2765. Springer, 2020.
- [29] Francesco dell’Isola, Pierre Seppecher, Mario Spagnuolo, Emilio Barchiesi, François Hild, Tomasz Lekszycki, Ivan Giorgio, Luca Placidi, Ugo Andreaus, Massimo Cuomo, Simon R. Eugster, Aron Pfaff, Klaus Hoschke, Ralph Langkemper, Emilio Turco, Rizacan Sarikaya, Aviral Misra, Michele De Angelo, Francesco D’Annibale, Amine Bouterf, Xavier Pinelli, Anil Misra, Boris Desmorat, Marek Pawlikowski, Corinne Dupuy, Daria Scerrato, Patrice Peyre, Marco Laudato, Luca Manzari, Peter Göransson, Christian Hesch, Sofia Hesch, Patrick Franciosi, Justin Dirrenberger, Florian Maurin, Zacharias Vangelatos, Costas Grigoropoulos, Vasileia Melissinaki, Maria Farsari, Wolfgang Müller, Bilen Emek Abali, Christian Liebold, Gregor Ganzosch, Philip Harrison, Rafał Drobnicki, Leonid Igumnov, Faris Alzahrani, and Tasawar Hayat.

Advances in pantographic structures: design, manufacturing, models, experiments and image analyses.  
*Continuum Mechanics and Thermodynamics*, 31(4):1231–1282, 2019.

- [30] Francesco dell’Isola, Pierre Seppecher, Jean Jacques Alibert, Tomasz Lekszycki, Roman Grygoruk, Marek Pawlikowski, David Steigmann, Ivan Giorgio, Ugo Andreaus, Emilio Turco, Maciej Gołaszewski, Nicola Rizzi, Claude Boutin, Victor A. Eremeyev, Anil Misra, Luca Placidi, Emilio Barchiesi, Leopoldo Greco, Massimo Cuomo, Antonio Cazzani, Alessandro Della Corte, Antonio Battista, Daria Scerrato, Inna Zurba Eremeeva, Yosra Rahali, Jean-François Ganghoffer, Wolfgang Müller, Gregor Ganzosch, Mario Spagnuolo, Aron Pfaff, Katarzyna Barcz, Klaus Hoschke, Jan Neggens, and François Hild.  
Pantographic metamaterials: an example of mathematically driven design and of its technological challenges.  
*Continuum Mechanics and Thermodynamics*, 31(4):851–884, 2019.
- [31] Anil Misra and Payam Poorsolhjouy.  
Identification of higher-order elastic constants for grain assemblies based upon granular micromechanics.  
*Mathematics and Mechanics of Complex Systems*, 3(3):285–308, 2015.
- [32] Jean-Jacques Alibert and Alessandro Della Corte.  
Homogenization of nonlinear inextensible pantographic structures by  $\gamma$ -convergence.  
*Mathematics and Mechanics of Complex Systems*, 7(1):1–24, 2019.
- [33] Y Rahali, I Giorgio, JF Ganghoffer, and F dell’Isola.  
Homogenization à la Piola produces second gradient continuum models for linear pantographic lattices.  
*International Journal of Engineering Science*, 97:148–172, 2015.
- [34] Jia Li.  
A micromechanics-based strain gradient damage model for fracture prediction of brittle materials—part i: Homogenization methodology and constitutive relations.  
*International journal of solids and structures*, 48(24):3336–3345, 2011.
- [35] Jia Li and Xiao-Bing Zhang.  
A numerical approach for the establishment of strain gradient constitutive relations in periodic heterogeneous materials.  
*European Journal of Mechanics-A/Solids*, 41:70–85, 2013.
- [36] Salma Barboura and Jia Li.  
Establishment of strain gradient constitutive relations by using asymptotic analysis and the finite element method for complex periodic microstructures.  
*International Journal of Solids and Structures*, 136:60–76, 2018.
- [37] Hua Yang, Bilen Emek Abali, Dmitry Timofeev, and Wolfgang H Müller.  
Determination of metamaterial parameters by means of a homogenization approach based on asymptotic analysis.  
*Continuum Mechanics and Thermodynamics*, pages 1–20, 2019.
- [38] Bilen Emek Abali and Emilio Barchiesi.  
Additive manufacturing introduced substructure and computational determination of metamaterials parameters by means of the asymptotic homogenization.  
*Continuum Mechanics and Thermodynamics*, pages 1–17, 2020.
- [39] B. E. Abali.  
Supply code for computations.  
<http://bilenekek.abali.org/>, 2020.
- [40] K. K. Mandadapu, B. E. Abali, and P. Papadopoulos.  
On the polar nature and invariance properties of a thermomechanical theory for continuum-on-continuum homogenization.  
*Mathematics and Mechanics of Solids*, pages 1–18, 2021.
- [41] Jeremy Bleyer.  
*Numerical Tours of Computational Mechanics with FEniCS*, 2018.
- [42] B. E. Abali.  
*Computational Reality*, volume 55 of *Advanced Structured Materials*.  
Springer Nature, Singapore, 2017.
- [43] Nicolas Auffray, Justin Dirrenberger, and Giuseppe Rosi.  
A complete description of bi-dimensional anisotropic strain-gradient elasticity.

- International Journal of Solids and Structures*, 69:195–206, 2015.
- [44] Nicolas Auffray, Regis Bouchet, and Yves Brechet.  
Derivation of anisotropic matrix for bi-dimensional strain-gradient elasticity behavior.  
*International Journal of Solids and Structures*, 46(2):440–454, 2009.
- [45] Nicolas Auffray, Hung Le Quang, and Qi-Chang He.  
Matrix representations for 3D strain-gradient elasticity.  
*Journal of the Mechanics and Physics of Solids*, 61(5):1202–1223, 2013.
- [46] Helmut J Böhm, Anton Eckschlager, and W Han.  
Multi-inclusion unit cell models for metal matrix composites with randomly oriented discontinuous reinforcements.  
*Computational materials science*, 25(1-2):42–53, 2002.
- [47] Francesco dell’Isola, Giulio Sciarra, and Stefano Vidoli.  
Generalized Hooke’s law for isotropic second gradient materials.  
*Proceedings of the Royal Society A: Mathematical, Physical and Engineering Sciences*, 465(2107):2177–2196, 2009.
- [48] Lidiia Nazarenko, Rainer Glüge, and Holm Altenbach.  
Positive definiteness in coupled strain gradient elasticity.  
*Continuum Mechanics and Thermodynamics*, pages 1–13, 2020.
- [49] Victor A Eremeyev, Sergey A Lurie, Yury O Solyaev, and Francesco dell’Isola.  
On the well posedness of static boundary value problem within the linear dilatational strain gradient elasticity.  
*Zeitschrift für angewandte Mathematik und Physik*, 71(6):1–16, 2020.
- [50] Hua Yang, Dmitry Timofeev, B Emek Abali, Baotong Li, and Wolfgang H Müller.  
Verification of strain gradient elasticity computation by analytical solutions.  
*ZAMM-Journal of Applied Mathematics and Mechanics/Zeitschrift für Angewandte Mathematik und Mechanik*, page e202100023, 2021.
- [51] B. E. Abali, W. H. Müller, and V. A. Eremeyev.  
Strain gradient elasticity with geometric nonlinearities and its computational evaluation.  
*Mechanics of Advanced Materials and Modern Processes*, 1(1):1–11, 2015.
- [52] B. E. Abali, W. H. Müller, and F. dell’Isola.  
Theory and computation of higher gradient elasticity theories based on action principles.  
*Archive of Applied Mechanics*, 87(9):1495–1510, 2017.
- [53] Sergei Khakalo, Viacheslav Balobanov, and Jarkko Niiranen.  
Modelling size-dependent bending, buckling and vibrations of 2d triangular lattices by strain gradient elasticity models: applications to sandwich beams and auxetics.  
*International Journal of Engineering Science*, 127:33–52, 2018.
- [54] Giuseppe Rosi and Nicolas Auffray.  
Anisotropic and dispersive wave propagation within strain-gradient framework.  
*Wave Motion*, 63:120–134, 2016.
- [55] Victor A Eremeyev, Giuseppe Rosi, and Salah Naili.  
Comparison of anti-plane surface waves in strain-gradient materials and materials with surface stresses.  
*Mathematics and mechanics of solids*, 24(8):2526–2535, 2019.
- [56] Muhammad Ridlo Erdata Nasution, Naoyuki Watanabe, Atsushi Kondo, and Arief Yudhanto.  
A novel asymptotic expansion homogenization analysis for 3-D composite with relieved periodicity in the thickness direction.  
*Composites science and technology*, 97:63–73, 2014.
- [57] Carlos M Portela, A Vidyasagar, Sebastian Krödel, Tamara Weissenbach, Daryl W Yee, Julia R Greer, and Dennis M Kochmann.  
Extreme mechanical resilience of self-assembled nanolabyrinthine materials.  
*Proceedings of the National Academy of Sciences*, 117(11):5686–5693, 2020.
- [58] Samuel Forest.  
Continuum thermomechanics of nonlinear micromorphic, strain and stress gradient media.  
*Philosophical Transactions of the Royal Society A*, 378(2170):20190169, 2020.

- [59] Khaled ElNady, Ibrahim Goda, and Jean-François Ganghoffer.  
Computation of the effective nonlinear mechanical response of lattice materials considering geometrical nonlinearities.  
*Computational Mechanics*, 58(6):957–979, 2016.